# Solar EUV Experiment (SEE): Mission overview and first results

Thomas N. Woods,[1] Francis G. Eparvier,[1] Scott M. Bailey,[2] Phillip C. Chamberlin,[1] Judith Lean,[3] Gary J. Rottman,[1] Stanley C. Solomon,[4] W. Kent Tobiska,[5] and Donald L. Woodraska[1]

Received 30 August 2004; revised 12 November 2004; accepted 30 November 2004; published 28 January 2005.

[1] The Solar EUV Experiment (SEE) is one of four scientific instruments on the NASA Thermosphere Ionosphere Mesosphere Energetics Dynamics (TIMED) spacecraft, which has been simultaneously observing the Sun and Earth's upper atmosphere since January 2002. The SEE instrument measures the irradiance of the highly variable, solar extreme ultraviolet (EUV) radiation, one of the major energy sources for the upper atmosphere. The primary SEE data product is the solar spectral irradiances from 0.1 to 194 nm in 1 nm intervals that are fundamental for the TIMED mission's investigation of the energetics in the tenuous, but highly variable, layers of the Earth's atmosphere above 60 km. The TIMED mission began normal operations on 22 January 2002, a time when the Sun displayed maximum levels of activity for solar cycle 23, and has provided daily measurements as solar activity has declined to moderate levels. Solar irradiance variability observed by SEE during the 2 years of the TIMED prime mission includes a variety of moderate and large flares over periods of seconds to hours and dozens of solar rotational cycles over a typical period of 27 days. The SEE flare measurements provide important, new results because of the simultaneous spectral coverage from 0.1 to 194 nm, albeit limited temporal coverage due to its 3% duty cycle. In addition, the SEE measurements reveal important, new results concerning phase shifts of 2–7 days in the intermediate-term variations between different UV wavelengths that appear to be related to their different center-to-limb variations. The new solar EUV irradiance time series from SEE are also important in filling the "EUV Hole," which is the gap in irradiance measurements in the EUV spectrum since the 1980s. The solar irradiances measured by SEE (Version 7, released July 2004) are compared with other measurements and predictions from models of the solar EUV irradiance. While the measurement comparisons show reasonable agreement, there are significant differences between SEE and some of the models in the EUV range. The data processing algorithms and calibrations are also discussed.

**Citation:** Woods, T. N., F. G. Eparvier, S. M. Bailey, P. C. Chamberlin, J. Lean, G. J. Rottman, S. C. Solomon, W. K. Tobiska, and D. L. Woodraska (2005), Solar EUV Experiment (SEE): Mission overview and first results, *J. Geophys. Res.*, *110*, A01312, doi:10.1029/2004JA010765.

## 1. Introduction

[2] Solar ultraviolet (UV) radiation at wavelengths less than 400 nm is an important source of energy for aeronomic processes throughout the solar system. Solar UV photons are absorbed in planetary atmospheres, as well as throughout the heliosphere, via photodissociation of molecules, photoionization of molecules and atoms, and photoexcitation including resonance scattering [e.g., see *Chamberlain*, 1978]. Nominal subdivisions of the UV spectral range are as follows: near ultraviolet (NUV) from 300 to 400 nm, middle ultraviolet (MUV) from 200 to 300 nm, far ultraviolet (FUV) from 120 to 200 nm, extreme ultraviolet (EUV) from 30 to 120 nm, X ray ultraviolet (XUV) from 1 and 30 nm, and X rays at wavelengths less than 1 nm. Solar EUV and XUV radiation photoionizes the neutral constituents of the atmospheres and participates in the formation of the ionosphere. The photoelectrons created in this process interact further with neutral species, leading to excitation, dissociation, and additional ionization. The excess energy from the absorption processes heats the atmosphere. As an example for Earth shown in Figure 1, solar MUV radiation heats the stratosphere, while solar UV radiation shortward of 170 nm heats the thermosphere. Atmospheric absorption of the solar UV radiation also initiates many chemical cycles, such as those

[1]Laboratory for Atmospheric and Space Physics, University of Colorado, Boulder, Colorado, USA.
[2]Geophysical Institute, University of Alaska, Fairbanks, Alaska, USA.
[3]Naval Research Laboratory, Washington, DC, USA.
[4]High Altitude Observatory, National Center for Atmospheric Research, Boulder, Colorado, USA.
[5]Space Environment Technologies, Pacific Palisades, California, USA.


0148-0227/05/2004JA010765$09.00

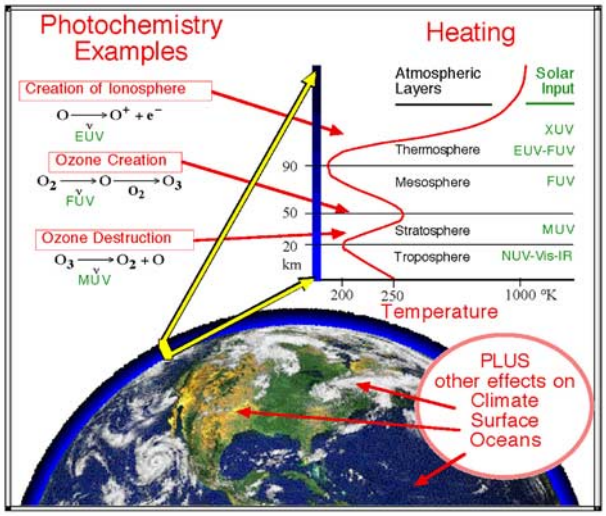


**Figure 1.** The solar UV radiation is a primary energy input to Earth's atmosphere. This radiation includes the middle UV (MUV: 200–300 nm), the far UV (FUV: 120–200 nm), the extreme UV (EUV: 30–120 nm), and the X ray UV (XUV: 1–30 nm). The photochemistry and heating of the atmosphere vary with altitude and are strongly dependent on the wavelength of the solar radiation and the absorption cross sections of the atmospheric species.

involving water vapor, ozone, nitric oxide, and chlorofluorocarbons in Earth's atmosphere [e.g., see *Brasseur and Solomon*, 1986]. As Figure 1 depicts, the chemistry cycle of ozone in Earth's stratosphere involves the creation of ozone via the photodissociation of molecular oxygen followed by the combination of the atomic oxygen with molecular oxygen and by the destruction of ozone via direct photodissociation. The longer wavelengths of the solar radiation, mainly from the NUV, visible (VIS: 400–700 nm), and near infrared (NIR: 700–10000 nm) spectral regions, are absorbed (and transmitted and reflected) by aerosols, clouds, and gases in the troposphere and by land surfaces and oceans; thus the Sun also affects those environments. All of these atmospheric processes are wavelength-dependent and are expected to be as variable as the intrinsic solar variability at the appropriate wavelengths.

[3] Accurate measurements of the solar UV spectral irradiance, along with an understanding of its variability, are therefore important for detailed studies of the atmospheric processes. The Solar EUV Experiment (SEE) aboard the TIMED spacecraft measures the solar spectral irradiance in the XUV, EUV, and FUV ranges. The TIMED satellite was launched on 7 December 2001, and daily measurements of the solar irradiance by SEE began on 22 January 2002. A summary of the SEE instrument, including calibrations and irradiance algorithms, and the results from the first 2 years of operations are the focus of this paper.

### 1.1. Nature of the Solar Variability

[4] The Sun varies on all time scales and the amount of variability is a strong function of wavelength. For this discussion, the solar irradiance is considered the full-disk solar intensity at 1 AU and does not include the 6.9% annual insolation factor due to Earth's changing distance from the Sun as a result of orbital eccentricity. Present understanding is that the intrinsic solar cycle variability is of the order of one-tenth of a percent in the visible portion of the spectrum. In the middle ultraviolet spectrum (200 to 300 nm), the amount of radiation decreases rapidly while the variability increases by an order of magnitude to a few percent. In the FUV and EUV ranges, the amount of radiation decreases further while the solar cycle variability continues to increase with the magnitude of the variation approaching a factor of two, for example at the H I Lyman-$\alpha$ emission at 121.6 nm, and an order of magnitude for the high-temperature coronal lines.

[5] Solar radiation shortward of 200 nm has a spectrum consisting of emission lines superimposed on the rapidly declining continuum. The emission lines arise in higher temperature layers of the outer solar atmosphere under non-LTE conditions and are strongly related to the magnetic activity of the Sun as seen, for example, in bright plages and the active network. It is known that these emission lines exhibit large amplitude variability during an 11-year solar cycle relative to the underlying FUV continuum. The XUV region is dominated completely by emission lines of primarily coronal origin that may vary by an order of magnitude during an 11-year solar cycle.

[6] Short-term irradiance variations, lasting from minutes to hours, occur during eruptive events on the Sun; intermediate term variations, modulated by the 27-day rotation period of the Sun, are related to the appearance and disappearance of active regions on the solar disk, and the more elusive long term variability is related to the 11-year Schwabe solar activity cycle, which in turn is related to the 22-year magnetic field cycle of the Sun [e.g., *Simon*, 1983]. The long-term variations in the XUV and EUV ranges have been poorly determined due to the lack of measurements and to the inadequate long-term accuracy of previous satellite solar instruments. Recent reviews about the solar EUV and UV variability with more details include those by *White* [1977], *Rottman* [1987], *Lean* [1987, 1991], *Tobiska* [1993], *Pap et al.* [1994], and *Woods et al.* [2004a].

### 1.2. Historical Context for SEE Observations

[7] Solar VUV measurements are only possible above the atmosphere and were first made photographically, and then by photometric detectors, on short duration rocket flights starting after the Second World War. The SOLRAD and AEROS satellites, Air Force Cambridge Research Laboratories rocket experiments, Orbiting Solar Observatory (OSO-3 and OSO-4) [*Hall and Hinteregger*, 1970; *Reeves and Parkinson*, 1970], and Atmospheric Explorer (AE-C, AE-D, and AE-E) [*Hinteregger et al.*, 1973] conducted survey observations through different parts of the spectrum during the 1960s and 1970s.

[8] Even today, the revised AE-E solar irradiance data representative of solar activity during solar cycle 21 [*Hinteregger et al.*, 1981; *Torr and Torr*, 1985] are routinely used in many atmospheric modeling studies (i.e., calculating photoelectron fluxes, heating, etc.). The absolute scale of the revised AE-E data set is based primarily on sounding rocket measurements rather than the satellite instruments because there were no provisions for in-flight calibrations of the solar instruments on AE-E [*Hinteregger et al.*, 1981].

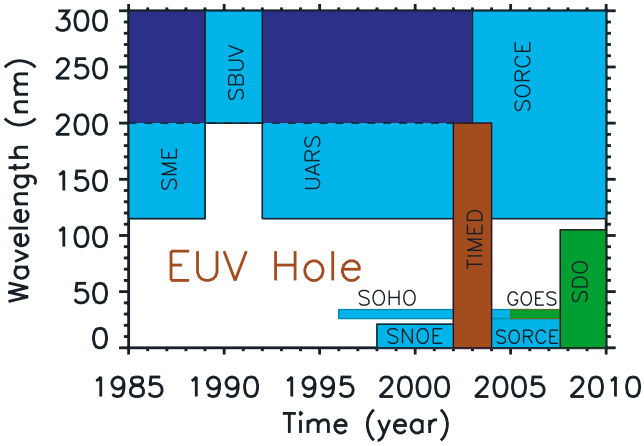


**Figure 2.** The Thermosphere Ionosphere Mesosphere Energetics Dynamics (TIMED) mission has begun to fill the "EUV Hole," being the time period when there have been very limited measurements of the solar EUV irradiance. There are a few other measurements, such as from sounding rockets, during this period, but the daily satellite measurements are only shown.

[9] The solar cycle variation of the EUV spectrum derived from these historical irradiance measurements was ambiguous [e.g., *Roble*, 1976; *Oster*, 1983] because of discrepancies in the absolute irradiance due to the AE-E instrument degradation and the inclusion of several different instruments [*Hinteregger et al.*, 1981; *Heroux and Higgins*, 1977; *Rottman*, 1987]. Recent solar FUV and MUV irradiance measurements from the Upper Atmosphere Research Satellite (UARS) have addressed this issue by including two independent instruments that have accurate preflight calibrations traceable to the National Institute of Standards and Technology (NIST) radiometric standards and also have in-flight calibrations to precisely track instrument degradation.

[10] Following the final AE-E measurements in 1981, there has been a long hiatus of solar EUV irradiance observations, referred to as the "solar EUV hole" [*Donnelly*, 1987]. The few solar EUV spectral irradiance observations made during this period include about 20 days during the 9-month mission of the San Marco 5 satellite [*Schmidtke et al.*, 1985; *Schmidtke et al.*, 1992], intermittent sounding rocket measurements [e.g., *Woods and Rottman*, 1990], and Voyager 1 and 2 measurements made a few days per year. Additionally, there have been several integrated EUV flux measurements from Pioneer Venus [*Brace et al.*, 1988], PHOBOS, SOHO Solar EUV Monitor (SEM) [*Judge et al.*, 1998], and sounding rocket measurements [e.g., *Ogawa et al.*, 1990]; however, these broadband integrated flux measurements are less useful for detailed solar-terrestrial studies.

[11] The new SEE measurements have begun to fill the "EUV Hole" as indicated in Figure 2. As shown in this figure, the solar UV irradiance longward of 115 nm has been measured almost continuously for the past two solar cycles and with an accuracy of 2–10% [e.g., *Woods et al.*, 1996]; consequently, the solar FUV and MUV irradiance variations are better understood than the solar EUV and XUV irradiance. The next NASA mission with full spectral coverage in the EUV range is the SDO mission having a planned launch in 2008.

### 1.3. SEE Science Objectives

[12] The SEE investigation contributes primarily to the NASA TIMED mission goal of characterizing the sources of energy responsible for the thermal structure of the mesosphere, the lower thermosphere, and the ionosphere (MLTI). These energy sources include solar electromagnetic radiation, solar energetic particles, Joule heating, conduction, dynamical forcing, and chemical energy release. Of these energy inputs, the solar vacuum ultraviolet (VUV) radiation below 200 nm is the dominant global energy source for heating the thermosphere, creating the ionosphere, and driving the diurnal cycles of wind and chemistry. Changes in the amount of solar VUV radiation result in corresponding changes in the energy balance of the upper atmosphere, dynamics, and photochemistry. A detailed quantitative understanding of the changes in the solar VUV irradiance and the basic state variables, temperature and densities of $N_2$, $O_2$, and O, are thus essential to detailed investigations of atmospheric energetics, dynamics, and chemistry.

[13] Solar cycle peak-to-peak variability near 200 nm is about 10% and increases at shorter wavelengths to typically a factor of 2 to 3 for chromospheric emissions and a factor of 5 or more for coronal emissions. Neither the magnitude of the irradiance nor the variability of these emissions are well understood, especially at the shortest wavelengths shortward of 40 nm. For upper atmosphere research, SEE provides the necessary solar VUV irradiance measurements from 0.1 to 195 nm with 0.4 nm spectral resolution longward of 27 nm and about 7 nm resolution shortward of 27 nm. The other three TIMED instruments and several ground-based instruments provide measurements of the basic state variables of the upper atmosphere over a range of altitudes from 50 to 400 km. Accurate measurements of the energy sources and the basic state variables permit unprecedented validation and refinement of atmospheric models of the MLTI, and those results will provide a precise quantification of the response of the upper atmosphere to the various energy sources.

[14] The SEE investigation also contributes to the TIMED mission goal of improving the understanding of those processes related to anthropogenic influences and the establishment of a baseline set of observations for future investigations. Distinguishing between the natural, predominantly solar-induced upper atmospheric variability, and anthropogenic influences in the MLTI regions, requires a baseline of solar VUV spectral irradiance and basic state variables with an accuracy of 20% or better (1-$\sigma$ value). Existing proxy models that employ ground-based measurements of solar activity to estimate the solar VUV irradiance are highly uncertain and lack the required accuracy for solar connection studies, as evidenced by the significant disagreement among them [*Lean et al.*, 2003]. Therefore the SEE investigation will also develop improved solar irradiance models, based on the TIMED SEE measurements, for future comparisons of natural and anthropogenic effects.

[15] The key elements in data analysis and modeling for the SEE investigation are the analysis of solar irradiance variability, the study of solar-terrestrial relationships using the measured solar irradiance as parameters in models of

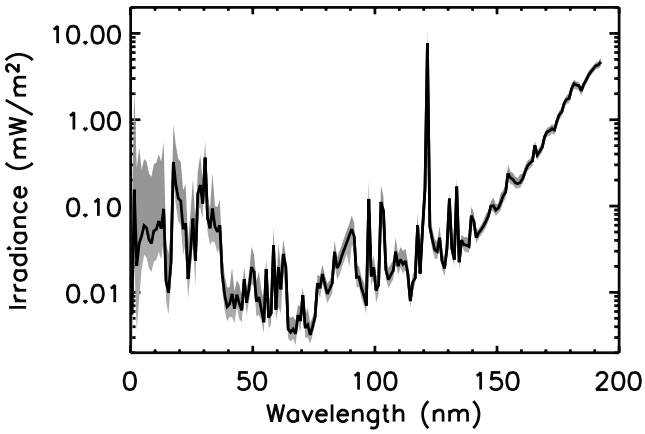


**Figure 3.** The 1-nm solar spectra from the Solar EUV Experiment (SEE) Level 3 data products (Version 7) are shown from February 2002 to February 2004. The middle (dark) spectrum is the median value, and the upper and lower (gray) ranges indicate the daily solar variability during this 2-year period. The flare variability observed by SEE is not included in this plot.

the atmosphere, the verification of atmospheric models and laboratory cross sections for atoms and molecules using measured solar absorption profiles from solar occultations, and the development of new generation models of the solar EUV irradiance. The primary atmospheric models for the SEE investigation are the Thermosphere Ionosphere Mesosphere Electrodynamics General Circulation Model (TIME-GCM) [*Roble et al.*, 1988], the MSISE-90 model [*Hedin*, 1991], and the NRLMSISE-00 model [*Picone et al.*, 2002].

[16] The primary data product from SEE is the daily average solar spectral irradiance from 0 to 195 nm in 1 nm intervals and with flares removed. This product is called the SEE Level 3 data product. The first research quality version of this SEE product is Version 6 released in February 2003. The latest SEE data set is Version 7, released in July 2004, and includes improved corrections for instrument responsivity changes and higher time cadence (hourly) data that are named the Level 3A data product that includes the flare data. The accuracy goal for the SEE data is 20%, and the measurement precision goal is 4%. Examples of the solar VUV spectra from the SEE Level 3 data products are shown in Figure 3. The vertical spread of these spectra arises primarily from variations of the solar irradiance during 2002 and 2003 with flares excluded.

## 2. Instrument Description

[17] The Solar EUV Experiment (SEE) includes two instruments that together measure the solar VUV spectral irradiance from 0.1 to 194 nm. The EUV Grating Spectrograph (EGS) is a normal incidence Rowland circle spectrograph with a spectral range of 27 to 194 nm and 0.4 nm spectral resolution. The XUV Photometer System (XPS) includes nine silicon XUV photodiodes with thin film filters deposited directly on the photodiodes. This XUV photometer set measures the solar irradiance from 0.1 to 27 nm with each filter having a spectral bandpass of about 7 nm. A more detailed description of the SEE instrument is given by *Woods et al.* [1998], and some preflight calibration results for the XPS and EGS are given by *Woods et al.* [1999a] and *Eparvier et al.* [2001], respectively.

### 2.1. EUV Grating Spectrograph

[18] The EUV Grating Spectrograph (EGS) is a normal-incidence 1/4 m Rowland circle design. The detector is an array detector so that a complete spectrum is obtained in a few seconds with the grating fixed. The spectral coverage is 27 to 194 nm with a 0.17 nm bandpass per anode on the detector. The effective spectral resolution is 0.4 nm. This moderately high resolution is important for resolving blended lines such as the H I Lyman-$\beta$ (102.6 nm) and O VI (103.2 and 103.8 nm) lines. A blazed, mechanically ruled grating from Hyperfine is used in the EGS in order to cover such a wide spectral range. To maximize the efficiency at the shortest wavelengths, the grating has a gold coating with sufficient reflectivity down to 25 nm.

[19] The array detector is a CODACON array detector developed by G. M. Lawrence at University of Colorado [*McClintock et al.*, 1982]. The CODACON detector uses a microchannel plate (MCP) and coded anode electronics for its readout. The array format is 64 $\times$ 1024, and each anode (pixel) is 100 $\mu$ tall (along the slit) by 25 $\mu$ wide (dispersion direction). The MCP is coated with Au that provides better dynamic range and serves as the photocathode. With no telescope, the images from the CODACON detector record solar spectra, not solar images. The detector electronics includes 32 charge amplifiers, a photon detection circuit, and dual memory buffers for accumulating photon events into an image and for reading out the previous image simultaneously.

[20] The EGS, which has one grating, one detector, and two entrance slits, is operated in such a way that there are two redundant channels. Specifically, the grating and detector can be illuminated on two separate areas. One illumination configuration is used for daily measurements, and the other illumination configuration is used for weekly calibration checks of the daily measurements. To achieve redundant channels from a single grating/detector system, two slits, each being 25 $\mu$ wide by 1 mm tall and offset 3 mm vertically from each other, are used to illuminate the detector differently. In addition, the optical axis is tilted by 2° to illuminate the grating differently. The SEE one-axis gimbal platform provides the means to tilt the optical axis relative to the Sun, and a slit selector mechanism is used to expose one of the two slits.

### 2.2. XUV Photometer System

[21] The XUV Photometer System (XPS) is a package of nine silicon XUV photodiodes for measuring the XUV and EUV irradiance. Each photodiode has a thin film filter to provide approximately 7 nm spectral bandpass. These thin film filters are deposited directly on the photodiode to avoid using metal foil filters which are more difficult to handle, prone to develop pin holes, and degrade with time. R. Korde of International Radiation Detectors, Inc. developed the silicon XUV photodiodes with thin film filters to have low noise and high long-term stability [*Korde and Geist*, 1987; *Korde et al.*, 1988; *Canfield et al.*, 1989; *Korde and Canfield*, 1989; *Canfield et al.*, 1994]. The National Insti-

tute for Standards and Technology (NIST) employs these Si XUV photodiodes as XUV standard detectors. The electronics for each XPS photodiode are simple and include only a current amplifier and a voltage-to-frequency converter (VFC).

[22] Several materials are suitable for use as XUV filters, and multiple coatings on the same diode provide a way to narrow the bandpass of each diode. *Powell et al.* [1990] discuss thin film filters suitable for this wavelength range. In addition to selecting the spectral bandpass, the filter must also block solar visible radiation by a factor of $10^{10}$ or better; otherwise, solar visible radiation (instead of the XUV radiation) dominates the XUV photometer signal. The thin film filters used on XPS photodiodes are Ti/C, Ti/Pd, Ti/Zr/C, Al/Sc/C, Al/Nb/C, Al/Cr, and Al/Nb. In addition, one bare Si photodiode is used with Acton Lyman-$\alpha$ filters to provide a measurement of the important solar Lyman-$\alpha$ emission.

[23] A set of 12 photodiodes is packaged together with a common filter wheel mechanism. Fused silica windows on the filter wheel mechanism permit accurate subtraction of the background signal from visible and near UV light. Nine photodiodes have filters for making solar XUV irradiance measurements, and three photodiodes are bare Si photodiodes to track the transmission of the fused silica windows. A typical measurement cycle for each XUV photometer measures the dark signal with no aperture, then the background signal with the window, and then the solar XUV radiation with a clear aperture.

[24] The only significant SEE instrument anomaly involves the XPS filter wheel, which became stuck in position 6 on day 2002/205. In this configuration, the XPS instrument has three solar XUV measurements (instead of its original nine). This anomaly creates a spectral gap of 11–27 nm for the current SEE observations, but this gap is filled in the SEE Version 7 data products. The SORCE XPS, which is almost identical to the TIMED SEE XPS, began making daily solar XUV irradiance measurements in March 2003, and the SEE Level 3 and 3A data products include the SORCE XPS results shortward of 27 nm starting on day 2003/070. Between days 2002/205 and 2003/070, the 11–27 nm gap is filled using the SEE XPS 0.1–7 nm channel (XP#1) as a proxy that is based on the earlier measurements by SEE XPS.

### 2.3. Other SEE Subsystems

[25] Additional subsystems to accommodate this solar investigation on the TIMED spacecraft include the SEE Solar Pointing Platform (SSPP), a one-axis gimbal platform for pointing the solar sensors toward the Sun, and the Microprocessor Unit (MU). With the SSPP controlling the solar pointing in only one axis, the SEE instruments have a wide field of view (>11°) so that the Sun drifts through the field of views for a few minutes each orbit. The SSPP has a range of motion of 190° and moves about 3° per day to account for satellite orbit precession and seasonal movement of the Sun. With its own pointing platform and Sun sensor with control and knowledge to better than 1 arcminute, SEE imposes minimal requirements on the spacecraft attitude control.

[26] The following characteristics are for the entire SEE system. The mass of SEE is 29 kg. The SEE operating power is 33 W, and the SEE data rate is 4 kb/s. The normal operating temperature range for SEE is 15 to 25°C.

### 2.4. SEE Observations

[27] The TIMED spacecraft was launched on 7 December 2001, and daily SEE measurements of the solar VUV irradiance began on 22 January 2002. Because of the configuration of SEE on the TIMED spacecraft, SEE observes the Sun for about 3 min per orbit (the TIMED orbital period is about 97 min). During each 3-min observation, SEE normally obtains twenty 10-s integrations while the Sun drifts through its ~12° field of view.

[28] The TIMED mission began at a time when solar activity was near maximum levels during solar cycle 23. By July 2004, solar activity had declined to moderate solar cycle levels. Solar irradiance variability observed by SEE during the first 2 years of operations includes a number of moderate and large flares over periods of seconds to hours and a few dozen solar rotational cycles over periods near 27 days. Because SEE obtains full spectral coverage within its normal solar observation of ~3 min, the SEE measurements provide a unique view of the flare response across the full VUV range (0–200 nm), albeit an intermittent view with its 3% duty cycle.

## 3. Instrument Calibrations and Characterizations

[29] A critical problem with many of the earlier solar VUV irradiance measurements is the lack of adequate accuracy and of the long-term relative accuracy from instrument degradation. The preflight and in-flight calibrations are therefore crucial components of the SEE program. The following sections give an overview of the calibration activities. More detailed descriptions of the preflight calibration results for the XPS and EGS are given by *Woods et al.* [1999a] and *Eparvier et al.* [2001], respectively. The various calibrations for the XPS instruments on TIMED satellite, SORCE satellite, and the SEE rocket calibration payload are described in more detail by T. N. Woods et al. (XUV Photometer System (XPS) 1: Overview and calibrations, submitted to *Solar Physics*, 2004).

### 3.1. Preflight Calibrations

[30] The preflight photometric calibrations of SEE include transferring to the instrument the calibrations of the National Institute of Standards and Technology (NIST) radiometric standards, such as reference photodiodes, radioactive X ray sources, and synchrotron radiation [*Walker et al.*, 1988; *Canfield and Swanson*, 1987; *Parr and Ebner*, 1987]. The current VUV calibration techniques are able to achieve an accuracy of about 3 to 7% (1-$\sigma$ value). The primary photometric standard for the SEE calibrations is the Synchrotron Ultraviolet Radiation Facility (SURF-III) at NIST in Gaithersburg, Maryland. The EGS is directly calibrated at SURF, and the XPS photodiodes are calibrated as a function of wavelength using a monochromator and reference photodiode at SURF and at the Physikalisch-Technische Bundesanstalt (PTB) electron storage ring called BESSY [*Scholze et al.*, 2001].

[31] Besides the fundamental responsivity calibrations, preflight characterizations are undertaken for several other important instrument parameters. The aperture areas are determined using a precision microscope to measure the

dimensions of the apertures, rectangular slits for EGS and round apertures for XPS. The response of the fully assembled instrument is mapped over its field of view (FOV) to precisely determine its uniformity. The gimbal tables at SURF are utilized to make detailed FOV maps for EGS as done for the UARS SOLSTICE and solar rocket instruments [*Woods et al.*, 1993; *Woods and Rottman*, 1990; *Woods et al.*, 1994]. A $12^\circ \times 12^\circ$ gimbal table at LASP is used to obtain the visible FOV maps for XPS. Linearity tests for EGS are performed using the capability to adjust the SURF electron beam current level over six orders of magnitude. Linearity tests for XPS electronics use a calibrated, adjustable current source in place of the photodiode. As needed for the calibration analyses, the detector dark signals are measured for all of these characterizations. The gain of the detectors is also determined over the operating temperature range ($-10^\circ$C to $40^\circ$C) and at different high-voltage (HV) settings for the CODACON detector.

[32] Because the EGS is a more complicated instrument than XPS, additional calibrations and characterizations are performed for the EGS. Higher grating order contributions are quantified at SURF using multiple beam energies to derive the responsivities of the first, second, and third orders [*Chamberlin et al.*, 2004]. These higher grating orders are only important between 40 and 115 nm because the Au-coated grating does not have significant responsivity shortward of 20 nm and because a $MgF_2$ window on the detector blocks higher orders longward of 115 nm. An important characterization for the CODACON detector is obtaining the pixel-to-pixel variations, called the flat-field (FF) calibration; FF images are obtained using an onboard mercury arc lamp that illuminates the detector directly. A careful analysis of the spectrograph's scattered light, which is primarily caused by the diffraction grating [*Woods et al.*, 1994], is also performed for EGS. The preflight wavelength calibrations for EGS incorporate measurements using the emission lines from deuterium and mercury arc lamps in the FUV range and the short wavelength cutoff edges of foil filters in the EUV range. Finally, the gain of the CODACON detector is determined as a function of time after turn-on because the gain of MCPs increases during warm up. These turn-on calibrations indicate that the EGS detector's HV power needs to be on for 20 min to give stable results. For this reason, the EGS detector is left on in-flight even though it only observes the Sun with a duty cycle of about 3%.

### 3.2. In-Flight Responsivity Tracking

[33] In addition to measuring the absolute value of the solar irradiance, determining the long-term variation of the irradiance is a fundamental scientific goal; therefore in-flight tracking of SEE's instrument responsivity is required. The in-flight tracking procedures include onboard redundant optical channels that are augmented by direct calibrations from instruments underflown on rockets (discussed below). The goal of this variety of techniques is to achieve long-term relative accuracy of SEE's solar irradiance of 10% uncertainty (1-$\sigma$ value).

[34] Both the EGS and XPS instruments have redundant optical channels. One channel is utilized for daily measurements, and the other is only used once a week to regularly provide a relative calibration for the other channel. Owing to the XPS filter wheel anomaly on day 2002/205 that is discussed more in section 2.2, the redundant XPS channel calibrations are limited to the early part of the TIMED mission. The SORCE XPS measurements starting in March 2003 now provide routine calibration checks for the SEE XPS instrument. The basic assumption for this technique is that exposure to the space environment and to solar radiation is major factor determining instrument degradation. The use of different duty cycles permit an evaluation of the instrument responsivity changes (typically degradation) as related to solar exposure rate. Maintaining a high level of cleanliness for the instruments greatly reduces the degradation related to contaminants on the optics [e.g., *Woods et al.*, 1999b].

[35] Other in-flight characterizations include wavelength calibrations for each EGS spectrum using the observed solar emission lines as reference wavelengths, flat-field measurements several times a week for the EGS detector, and field of view maps every 2 months by scanning the Sun across different parts of the optics and detectors. These in-flight tests confirm similar preflight calibration measurements and ensure that the SEE data processing utilizes the most accurate instrumental parameters. Many of these in-flight test results are used directly in the SEE data processing software.

### 3.3. Rocket Underflight Experiment

[36] Independent measurements of the solar VUV spectral irradiance by SEE prototype instruments flown on sounding rockets provide a calibration for the in-flight SEE observations. These underflight measurements, made approximately annually, are crucial because they provide regular absolute in-flight calibration for the SEE instruments, as the redundant channels themselves can degrade.

[37] The rockets are launched from the NASA facility at the White Sands Missile Range in New Mexico and are supported by the NASA Sounding Rocket Operations Contract (NSROC). Preflight and postflight calibrations of the prototype instrument are performed at NIST SURF-III for each calibration rocket flight.

[38] The first rocket calibration experiment with its preflight and postflight calibrations at SURF provides a fresh calibration for the SEE instrument whose responsivity could have changed between its last preflight calibration in May 2000 and being launched in December 2001. For this reason, the first rocket calibration experiment was flown as soon as possible after activating the SEE instrument in January 2002. The results from the rocket calibration experiment flown on 8 February 2002 (day 2002/039) are incorporated into the SEE Version 6 data products; that is, the responsivity parameters used in data processing were adjusted so the SEE irradiance results on 2002/039 agreed with the rocket irradiances. Because the instrument degradation function is not well known before this date, the released SEE data products start with the data on day 2002/039. The second calibration rocket for SEE was launched on 12 August 2003, and those results are included in the SEE Version 7 data products. The third calibration rocket for SEE was launched on 15 October 2004, and those results will be included in the future SEE Version 8 data products.

[39] The rocket XPS calibration is based on responsivity calibrations of the individual XUV photodiodes and elec-

**Table 1.** List of Thermosphere Ionosphere Mesosphere Energetics Dynamics (TIMED) Solar EUV Experiment's (SEE's) Public Data Products[a]

| Data Product | λ Range, nm | Δt Average | Description |
|---|---|---|---|
| EGS L2 | 27–194 | Day | EGS solar irradiance at instrument resolution |
| EGS L2A | 27–194 | Orbit | EGS solar irradiance at instrument resolution |
| XPS L2 | 0–27 | Day | XPS solar irradiance at instrument resolution |
| XPS L2A | 0–27 | Orbit | XPS solar irradiance at instrument resolution |
| SEE L3 | 0–194 | Day | Solar irradiance in 1-nm intervals and extracted emission lines |
| SEE L3A | 0–194 | Orbit | Solar irradiance in 1-nm intervals and extracted emission lines |

[a]EGS, EUV Grating Spectrograph; XPS, XUV Photometer System.

tronics gain calibrations as done for the SEE XPS instrument. The photodiode calibrations in 2002 were performed between 5 and 35 nm by R. Vest at NIST using reference detectors with a monochromator at SURF-III [*Canfield et al.*, 1994]. These diode responsivity results are then modeled to obtain the diode filter material thickness, and finally the filter model is used to extend the calibration results to shortward of 5 nm and at higher spectral resolution. These modeled calibration results at the shorter wavelengths are consistent with the BESSY calibration results between 0.8 nm and 5 nm for photodiodes calibrated at both locations. The rocket XPS calibrations in 2003 were performed using the SURF-III synchrotron beam directly. For this technique, multiple electron beam energies that have different spectral radiance profiles provide a responsivity calibration that is obtained as a function of wavelength by modeling the diode filter material thickness. Both calibration techniques gave very similar results, but the more direct calibration with the synchrotron radiation is easier to implement because it does not require disassembly of XPS. Partly because of the intermediate modeling of the filters for the XPS responsivity, the uncertainty for the rocket XPS irradiances is 15–20%.

[40] The rocket EGS calibration is primarily performed at SURF-III using the Beam Line 2 (BL-2) facility as was done for the SEE EGS. The many different calibrations, as described earlier for the SEE EGS in section 3.1, are also performed for the rocket EGS. Because of the different responsivity across the EGS spectral range, the EGS calibrations are subdivided into EUV calibrations (27–115 nm) and FUV calibrations (129–194 nm). The FUV calibrations are performed using a $CaF_2$ window in the beam line in order to increase the FUV signal without exposing the detector to EUV radiation; two windows are employed so that the transmission of each window is obtained as part of the calibration. The EUV calibrations are performed without any filters in the beam line. The EGS Lyman-α filter (115–129 nm), which decreases the radiation by a factor of 100, is not well calibrated at SURF, so the rocket XPS and UARS Lyman-α measurements are used for calibrating the EGS Lyman-α region. *Chamberlin et al.* [2004] give the details of the calibrations for the rocket EGS and the results for the February 2002 rocket observation.

[41] The EUV calibrations for the rocket EGS are substantially improved over those of the SEE EGS because the higher-order contributions are more accurately obtained. This improvement was achieved by performing the multiple beam energy calibrations at each FOV map position without moving the SURF gimbal tables, whereas the original EGS calibrations were obtained over the full FOV map for each beam energy. Because the SURF gimbal tables have an accuracy of about 1 arc-minute, the original EGS calibrations at different beam energies are not exactly at the same optical positions and thus introduced additional uncertainties. Furthermore, seven different beam energies were used for calibrating the rocket EGS, and only three different beam energies were used for the SEE EGS. While a minimum of three beam energies is required to obtain the contributions from three grating orders, the additional beam energy calibrations permit a selection of the best three beam energies for analysis. *Woods and Rottman* [1990] and *Chamberlin et al.* [2004] describe the techniques to extract responsivities for different grating orders using different SURF beam energies.

## 4. Data Processing

[42] The SEE data are processed from raw units of counts per second to irradiance units using straightforward conversion equations. There are eight primary SEE data products: EGS Level 1, XPS Level 1, EGS Level 2, and 2A, XPS Level 2 and 2A, and SEE Level 3 and 3A. These data products of the solar irradiance are produced on a daily basis and, except for the Level 1 products, are available to the public from http://see.colorado.edu/see/. These six public data products are listed in Table 1. The Level 1 data products are the irradiances of each measurement usually taken with a 10-s integration period and at instrument spectral resolution. All of the degradation corrections are not applied to the Level 1 data, and so they are not publicly available. The Level 2 data products are the irradiances averaged over the day, at 1 AU, and at instrument spectral resolution. The Level 2A data products are the irradiances averaged over the 3-min solar observation during each orbit. These averages are taken as the median values, which are less sensitive than is the mean to large, short-term deviations such as from flares. The averages for the EGS L2 and L2A data are produced after the EGS Level 1 data are regridded into 0.1 nm intervals. Only high-fidelity data are used for the Level 2 data products; data removed include those taken in the South Atlantic Anomaly (SAA) or near the FOV edges, solar occultation data, and any data identified outside calibrated ranges such as temperature.

[43] The SEE Level 3 data product is generated by combining the EGS and XPS Level 2 results with the EGS used longward of 27 nm and XPS shortward of 27 nm. The Level 3 product includes the solar spectrum in 1 nm intervals on 0.5 nm centers, the irradiances of 38 emission lines extracted from the EGS spectrum and with the background continuum removed, and the irradiances from the individual

**Table 2.** List of Gaps for SEE's Daily Data Products[a]

| Date, YYYY/DOY | EGS L2 | XPS L2 | SEE L3 | Reason for Gap |
|---|---|---|---|---|
| 2002/061 | X | X | X | Spacecraft Safehold |
| 2002/063 | X | | SG | EGS Exp. Load Error |
| 2002/206–210 | | X | SG | XPS Filter Anomaly |

[a]An "X" indicates that there are no data for this data product. A "SG" indicates that there are spectral gaps in this data product.

XPS photometers. The new data products available with the SEE Version 7 release include the orbit average solar irradiances as Level 2A (instrument resolution) and Level 3A (1-nm intervals) data products. The orbit averages are from 3-min observations with a repeat rate of about 97 min, that is with a duty cycle of 3%. These Level 2A and 3A (orbit average) data products were recently added to assist in the analysis of the many flares observed so far during the TIMED mission.

[44] The Level 2, 2A, 3, and 3A data products are made available to the public on the SEE web/ftp site (http://lasp.colorado.edu/see/) about 4 days after the data are obtained. These data products are stored as NetCDF files, and reader procedures written in the Interactive Data Language (IDL) are also available on the web/ftp site. The few data gaps for the SEE data products are listed in Table 2. Owing to the ongoing analysis of instrument degradation, caution is needed when using the most recent SEE data because they are generally not yet validated with the in-flight calibration experiments, some of which are made on a weekly basis, some on a 2-month basis, and some with the underflight rocket calibration experiment flown annually. The following sections describe the algorithms used in the Version 7 of the SEE data-processing code.

### 4.1. EGS Algorithms

[45] The following algorithm describes the derivation of the solar irradiance, $E$, used in SEE EGS Level 1 data processing code. This algorithm is a straightforward calculation using equation (1) as a function of count rates, $C$, at each detector anode position, $a$. The wavelength, $\lambda$, is also a function of anode position, and this relationship is determined for each solar spectrum using the brighter, isolated emission lines as reference wavelengths.

$$E(a) = \frac{C'(a) - SL(a, C') - OS(a, C')}{A \cdot \Delta\lambda \cdot R_c(a) \cdot f_{FOV}(a, x, y)} \cdot \frac{h \cdot c}{\lambda} \tag{1a}$$

$$C'(a) = (C_{cor}(a) \cdot L(C_{cor}) - D) \cdot G(HV, T) \tag{1b}$$

$$C_{cor}(a) = C(a) \cdot FF(a) \cdot f_{Degrade}(a, t). \tag{1c}$$

[46] The corrected count rates, $C'$, includes corrections for the dark (background) signal, $D$, the flat-field variations of the array detector, $FF$, the nonlinearity response at high count rates, $L$, the gain of the detector as a function of high voltage setting and temperature, $G$, and the degradation function, $f_{\mathrm{Degrade}}$. The other corrections include the scattered light, $SL$, the slit area, $A$, the bandpass, $\Delta\lambda$, the responsivity at the center of the field of view (FOV), $R_c$, the FOV factor at offset position $(x, y)$, $f_{\mathrm{FOV}}$, and the order sorting for removing the lines at 2nd and 3rd grating orders, $OS$. The irradiance is reported in units of W m$^{-2}$ nm$^{-1}$, and thus the $hc/\lambda$ factor is included for the photon energy conversion. The responsivity for EGS, as shown in Figure 4, peaks in the EUV region and has a logarithmic decrease into the FUV region.

[47] The measurement precision, being the uncertainty for a single measurement, is given by equation (2). These uncertainties are specified as fractional uncertainties and are thus unitless. The typical measurement precision is about 3%.

$$\sigma_{meas} = \frac{\sqrt{\sigma_{C'}^2 \bullet C'^2 + \sigma_{SL}^2 \bullet SL^2 + \sigma_{OS}^2 \bullet OS^2}}{C' - SL - OS} \tag{2a}$$

$$\sigma_{C'} = \sqrt{\sigma_C^2 + \sigma_{FF}^2 + \sigma_L^2 + \sigma_G^2 + \sigma_{\mathrm{deg}\,rade}^2}. \tag{2b}$$

[48] The accuracy, being the uncertainty for the absolute value of the irradiance from a single measurement, is given by equation (3). The largest source of uncertainty for the EGS irradiance accuracy is the uncertainty of the preflight responsivity, which typically is about 7%. As indicated in Figure 4, the uncertainty of the responsivity increases rapidly below 32 nm.

$$\sigma_E = \sqrt{\sigma_{meas}^2 + \sigma_A^2 + \sigma_{\Delta\lambda}^2 + \sigma_R^2 + \sigma_{FOV}^2 + \sigma_\lambda^2}. \tag{3}$$

[49] The degradation of the EGS is actually tracked through three functions: flat-field images ($FF$), weekly degradation ($f_{\mathrm{Degrade}}$), and annual rocket calibrations (adjusted $R_C$). The flat-field function, $FF$, is actually the flat-field images taken during the previous week that is normalized using the preflight flat-field image. The flat-field function therefore includes the local degradation on the

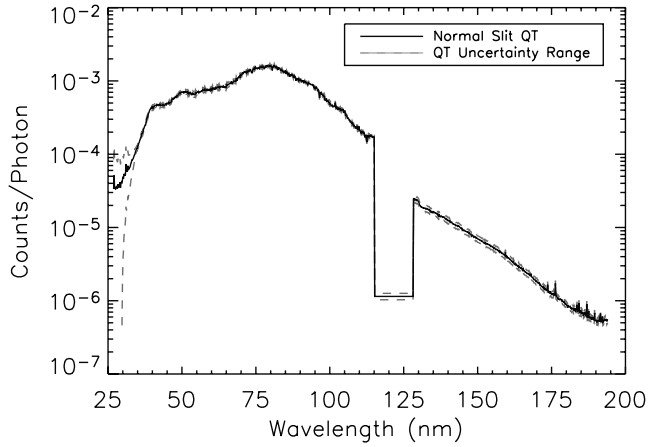


**Figure 4.** The EUV Grating Spectrograph (EGS) responsivity, also called the quantum throughput (QT), is shown for the center of its field of view. The uncertainty range for the QT is shown as the dashed lines. The decrease at 116–128 nm is due to a special filter in the detector so the bright H I Lyman-$\alpha$ (121.6 nm) emission would not saturate the EGS detector.

MCP that occurs primarily at the brighter emissions. The weekly degradation function is derived using trends in the ratios of the normal slit irradiances to the calibration slit irradiances, which are taken each Monday. For transfer of the rocket EGS results to SEE EGS, the responsivity, $R$, is adjusted for the SEE EGS so that its irradiance on 2002/039 matches the rocket EGS irradiance, and the uncertainty of the responsivity is updated to represent this transfer of calibration from the rocket EGS. For the later rocket flights, the EGS degradation function is a linear function of time in the EUV range. As discussed more in section 6.3, the EGS responsivity in the FUV range and in part of the EUV range is surprisingly increasing and is fit with an exponential function of time.

### 4.2. XPS Algorithms

[50] The following algorithm describes the irradiance derivation used in SEE XPS Level 1 data processing code. The algorithm to calculate the solar irradiance, $E$, is a straightforward calculation using equation (4) for the XPS photometer "i" when it is at a filter position with a clear aperture. Not shown in this equation is the conversion of the XPS raw data of counts per second to current, $I$, in units of nA. This current conversion includes preflight calibration parameters of the electrometer, and these parameters are a function of temperature. Basically, the irradiance is the photometer XUV current, being the total current corrected for its dark current and visible light current, divided by the responsivity factors, $f$ and $T$, and aperture area, $A$. The dark current and visible light current are measured when the photometer is at a filter position with a blocked (dark) aperture and an aperture with a fused silica window (visible), respectively. The visible light current is also corrected for the window transmission, which is also measured as part of the solar observation with a bare Si photodiode. The constant $k_E$ is included to convert the irradiance into energy units of W m$^{-2}$.

$$E_i = \frac{\left(I_{i,total} - I_{i,dark} - I_{i,visible}\right)}{f_{i,E\_total} \bullet \langle T_{i,xuv} \rangle \bullet A_i \bullet f_{i,xuv\_fov}} \bullet k_E \bullet f_{Degrade} \quad (4a)$$

$$I_{i,visible} = \frac{\left(I_{i,window} - I_{i,dark}\right)}{T_{window}} \bullet \frac{f_{i,clr\_fov}(\alpha_{xuv}, \beta_{xuv})}{f_{i,vis\_fov}(\alpha_{window}, \beta_{window})} \quad (4b)$$

$$T_{window} = \frac{\left(I_{b,window} - I_{b,dark}\right)}{\left(I_{b,clear} - I_{b,dark}\right)} \bullet \frac{f_{b,clr\_fov}(\alpha_{clear}, \beta_{clear})}{f_{b,vis\_fov}(\alpha_{window}, \beta_{window})} \quad (4c)$$

$$f_{i,E\_total} = \frac{\int_0^\infty T \bullet E \bullet d\lambda}{\int_{\lambda_1}^{\lambda_2} T \bullet E \bullet d\lambda} \quad (4d)$$

$$\langle T_{i,xuv} \rangle = \frac{\int_{\lambda_1}^{\lambda_2} T \bullet E \bullet d\lambda}{\int_{\lambda_1}^{\lambda_2} E \bullet d\lambda}. \quad (4e)$$

[51] There are three responsivity parameters used in equation (4). As given by equation (4d), the $f_{\mathrm{E\_total}}$ is the inverse fraction of the photometer signal in the photometer bandpass, $\lambda_1$–$\lambda_2$, and is a number greater than unity. The calculation of this fraction uses the preflight calibration transmission, $T$, and a modeled solar irradiance spectrum. This fraction changes depending on which solar spectrum is applied. This fraction is averaged over different solar conditions by using the flare spectrum and preflare spectrum from the NRLEUV model [*Meier et al.*, 2002; *Warren et al.*, 2001]. The uncertainty of this fraction is assumed to be the range of values of the fraction using different modeled spectra in the calculation. As given by the equation (4e), the $\langle T_{\mathrm{XUV}} \rangle$ is the transmission of the XUV filter weighted with the modeled irradiance spectrum. The uncertainty for the weighted transmission is assumed to be the range of values derived using different modeled spectra.

**Table 3.** List of XPS Responsivity Parameters[a]

| XP# | Filter | Δλ, nm | $\langle T \rangle$ | $f$ |
|---|---|---|---|---|
| 1 | Ti/C #14 | 0.1–7 | 0.1242 | 1.015 |
| 2 | Ti/C #10 | 0.1–7 | 0.1294 | 1.016 |
| 3 | Al/Sc/C #24 | 17–23 | 0.2214 | 1.725 |
| | | 0.1–7 | 0.3955 | 2.950 |
| 5 | Ti/Pd #17 | 0.1–10 | 0.1426 | 1.005 |
| 6 | Ti/Zr/Au #4 | 0.1–10 | 0.0304 | 1.013 |
| 7 | Al/Nb/C #3 | 17–21 | 0.0425 | 3.445 |
| | | 0.1–7 | 0.2414 | 1.500 |
| 9 | Al/Mn #6 | 0.1–7 | 0.1609 | 1.134 |
| | | 25–34 | 0.0069 | 11.51 |
| 10 | Al/Cr #7 | 0.1–7 | 0.1910 | 1.193 |
| | | 28–34 | 0.0157 | 8.298 |
| 11 | Ly-α × 2 | 121–122 | 0.00186 | 1.024 |

[a]The weighted transmission, $\langle T \rangle$, and the fraction of bandpass, $f$, are listed for the nine XUV Photometers (XP). Some photometers have a second bandpass, but only the parameters listed for the first bandpass are used in data processing. The XP# 4, 8, and 12 are bare Si diodes that measure the visible transmission of the fused silica filters and not included in this listing, as they do not obtain irradiance values.

[52] The $f_{\mathrm{xuv\_fov}}$ is the XUV field of view (FOV) factor relative to the center point responsivity and is a value near unity. The FOV factors in equation (4) are expressed as a function of yaw (α) and pitch (β) angles relative to the center of the FOV. The FOV factor is derived from the in-flight FOV map experiments and has an uncertainty proportional to the measurement precision. The values for the $\langle T \rangle$ and $f$ responsivity parameters for the nine XPS photometers are given in Table 3. The XP#3, 7, 9, and 10 also have the parameters for a second bandpass listed in Table 3, but only the parameters from the first bandpass are used by the SEE data processing software.

[53] The measurement precision, being the uncertainty for a single measurement, is given by equation (5). These uncertainties are specified as fractional uncertainties and are thus unitless. The uncertainty for the current conversion is less than 1%, and the typical measurement precision is about 1%.

$$\sigma_{meas} = \frac{\sqrt{\sigma^2_{total} \bullet I^2_{total} + \sigma^2_{dark} \bullet I^2_{dark} + \sigma^2_{visible} \bullet I^2_{visible}}}{I_{total} - I_{dark} - I_{visible}} \quad (5a)$$

$$\sigma_{\mathrm{visible}} = \sqrt{\sigma^2_{\mathrm{w-d}} + \sigma^2_{\mathrm{T_w}} + \sigma^2_{\mathrm{fov_{vis}}}(\mathrm{xuv}) + \sigma^2_{\mathrm{fov_{vis}}}(\mathrm{window})} \quad (5b)$$

$$\sigma_{w-d} = \frac{\sqrt{\sigma^2_{window} \bullet I^2_{window} + \sigma^2_{dark} \bullet I^2_{dark}}}{I_{window} - I_{dark}}. \quad (5c)$$

[54] The accuracy, being the uncertainty for the absolute value of the irradiance from a single measurement, is given by equation (6). The largest source of uncertainty for the irradiance accuracy is the uncertainty of the fraction factor, $f_{\mathrm{E\_total}}$, which ranges from 5% to 25%.

$$\sigma_E = \sqrt{\sigma^2_{meas} + \sigma^2_A + \sigma^2_{fov_{xuv}} + \sigma^2_{f_{E\_total}} + \sigma^2_{\langle T_{XUV}\rangle}}. \quad (6)$$

[55] The degradation of the XPS is tracked through two functions: weekly degradation ($f_{\mathrm{Degrade}}$) and annual rocket calibrations (adjusted $\langle T_{\mathrm{XUV}}\rangle$). Until the XPS filter wheel anomaly on day 2002/205, the weekly degradation function is derived using trends in the ratios of the daily photometer irradiances to the calibration photometer irradiances, which are taken each Monday. These trends up to day 2002/205 indicate no degradation for any of the XPS photometers. The XPS Lyman-$\alpha$ photometer might have a slight degradation that is presently uncorrected in the XPS data products. After the filter wheel anomaly, the weekly degradation function cannot be generated using this technique. However, we have noticed that the responsivity in the center of the FOV, which is exposed the most, has decreased relative to the outer angles; therefore this information can provide an indication of photometer degradation. A rough estimate of this degradation since day 2002/205 was included in XPS Version 6 data products, but a more refined model of the degradation, along with the SORCE XPS comparisons, are included in the XPS Version 7 data products. For transfer of the rocket XPS results to SEE XPS, the transmission parameter, $\langle T_{\mathrm{XUV}}\rangle$, is adjusted for the SEE XPS so that its irradiance on 2002/039 matches the rocket XPS irradiance.

[56] A different algorithm is used for the SEE Level 3 data products in deriving the 1-nm XUV spectra from the XPS measurements. Because the XPS measurements are broadband, a spectral model of the solar irradiance at 1-nm resolution is scaled to match the XPS measurement. The model used is an empirical proxy model called VUV2002 that is based on the reference spectra established before TIMED was launched and is parameterized with the daily $F_{10.7}$ and smoothed $F_{10.7}$ [*Woods and Rottman*, 2002]. This XPS processing algorithm is similar to the data processing technique used by the SNOE SXP. The scale factors are determined using the following equations for the bands at 0–4 nm, 4–14 nm, and 14–27 nm.

$$I_{predict} = \int_0^{\infty} R(\lambda) \bullet E(\lambda) \bullet d\lambda \quad (7a)$$

$$I_{measure} = \int_0^{\lambda_1} R(\lambda) \bullet E(\lambda) \bullet d\lambda + SF \bullet \int_{\lambda_1}^{\lambda_2} R(\lambda) \bullet E(\lambda) \bullet d\lambda + \int_{\lambda_2}^{\infty} R(\lambda) \bullet E(\lambda) \bullet d\lambda. \quad (7b)$$

[57] The responsivity function, $R$, of a photodiode, that includes all of the instrument corrections such as field of view and aperture area, is convolved with the model solar spectrum to determine the predicted current in equation (7a). Equation (4) and equation (7a) are equivalent following the relationship of parameters given in equation (8) for the responsivity, $R$.

$$R = \frac{T \bullet A \bullet f_{xuv\_fov}}{k_E \bullet f_{\mathrm{deg}rade}}. \quad (8)$$

[58] The scale factor, $SF$, for a spectral band, $\lambda_1$–$\lambda_2$, is determined using the measured XUV current as compared with the predicted current but with a scale factor applied as shown in equation (7b). The measured XUV current is the total current minus the dark current and minus the visible current. The scale factor for the 0–4 nm band is first determined. For the scale factors at the other bands, the scale factors from the shorter wavelength bands are first applied to the solar irradiance model spectrum. That is, the 4–14 nm scale factor is calculated using the 0–4 nm scale factor, and the 14–27 nm scale factor is calculated using the other two scale factors.

[59] This algorithm is used for both the TIMED SEE XPS and SORCE XPS, with the SEE Level 3 data products including the SORCE results after day 2003/070. The photodiodes from TIMED SEE that are used for the scale factors at 0–4 nm, 4–14 nm, and 14–27 nm are XP#1, #5, and #7, respectively. The photodiodes from SORCE XPS that are used for the same scale factors are XP#2 (Ti/C), #6 (Ti/Mo/Au), and #3 (Al/Sc/C), respectively. These SORCE photodiodes have very similar bandpasses as the corresponding TIMED SEE XPS photodiodes. After day 2002/205, the TIMED SEE XP#7 does not provide an XUV measurement due to the XPS filter wheel anomaly (stuck in position 6), and so an empirical relationship between SEE XP#7 and XP#1 prior to day 2002/205 is used to predict the SEE XP#7 current after day 2002/205. The predicted XP#7 current is then used to fill the Level 3 spectrum in the 14–27 nm range using the above scale factor algorithm.

[60] This scale factor algorithm that is only used in Level 3 processing is especially better for determining the flare spectra because it permits the model spectrum to change in broad bands. During nonflare periods, the two different algorithms provide the same irradiances to within 10%. However, during flare events the direct irradiance algorithm represented by equation (4) over predicts the irradiance at the longer wavelengths, namely in the 14–27 nm range. This over-prediction is due primarily to the $f_{\mathrm{E\_total}}$ ratio in equation (4) increasing dramatically for the long-wavelength photometers (e.g., XP#3, #7) when one uses a flare spectrum in modeling this parameter, but only a constant value for the $f_{\mathrm{E\_total}}$ ratio is used in equation (4). This algorithm was initially used in SEE Level 3 data processing, but as of Version 7, the SEE Level 3 data processing now uses the more accurate scale factor algorithm (equation (7)) for the solar XUV spectral irradiance in the 0–27 nm range. The selection of the XUV bands is based partially on the prediction of significant hot corona emissions during flares in the 0–4 nm and 9–13 nm regions [*Mewe and Gronenschild*, 1981; *Mewe et al.*, 1985; *Mewe et al.*, 1986].

## 5. Solar VUV Irradiance Variability

[61] The following sections discuss selected results concerning flare, solar rotation, and solar cycle variations

observed by SEE during the first 2 years of the TIMED mission.

### 5.1. Flare Variations

[62] There is, on average, one modest M-class flare every 2 days and one large X-class flare per month as determined from a survey of flares during solar cycles 21 and 22 [*Garcia*, 2000]. Flares occur more frequently during solar maximum conditions (i.e., during the first 2 years of the TIMED mission) than at solar minimum. Most solar flares affect the solar irradiance primarily in the X-ray spectrum, but sometimes a large flare can affect the solar VUV irradiance over a broad wavelength range up to 180 nm [e.g., *Brekke et al.*, 1996; *Woods et al.*, 2004a; *Meier et al.*, 2002]. Flares and the associated response of Earth's upper atmosphere to these abrupt events are an important aspect of space weather studies such as space-based communication/navigation systems. The solar EUV irradiance is needed on timescales of seconds to hours to improve the understanding of how flares cause abrupt space weather changes (e.g., sudden ionospheric disturbances or SIDs). The SEE flare measurements provide new information about the solar VUV irradiance changes during a flare and are contributing new understanding of the effects that flares could have on Earth's atmosphere.

[63] Because of its low duty cycle (3%), SEE observes only a few of all solar flares. Nonetheless, SEE has observed 14 large X-class flares and over 180 other flares. Many of these flares occurred during two periods in 2003; one period is late May and June and another is October and early November. The later period was more intense with the X17 flare on 28 October and the X28 (or larger) flare on 4 November. The dates and times of the 15 largest flares observed by SEE are listed in Table 4.

[64] The time series of the flare measurements by SEE are shown in Figure 5 as the 30-day running mean of the XPS and EGS flare indices that are part of the SEE Level 3A data product. Similar to the GOES flare index for the 0.1–0.8 nm irradiance, an XPS flare index is derived as the ratio of the 0.1–7 nm irradiance to the minimum irradiance for each day. EGS flare indices are similarly derived as the average of the flare-to-minimum ratios for the Si XII emission lines

**Table 4.** List of Large Flares Observed by SEE[a]

| SEE Observation Date/Time, UT | GOES Class (Peak Time) | Flare Ratio 0.1–7 nm | Flare Ratio 102.5 nm | EUV Norm Factor |
|---|---|---|---|---|
| 4/21/02 0213 | X1.5 (0151) | 8.3 | 1.10 | 8.9 |
| 7/23/02 0051 | X4.8 (0035) | 7.8 | 1.14 | 8.8 |
| 8/24/02 0138 | X3.1 (0112) | 5.9 | 1.07 | 19.6 |
| 5/27/03 2310 | X1.3 (2307) | 12.1 | 1.26 | 4.0 |
| 5/29/03 0105 | X1.2 (0105) | 8.5 | 1.38 | 3.6 |
| 6/17/03 2259 | M6.8 (2258) | 6.4 | 0.98 | 11.2 |
| 10/26/03 0729 | X1.2 (0654) | 4.6 | 1.08 | 8.7 |
| 10/26/03 1850 | X1.2 (1819) | 6.6 | 1.07 | 7.4 |
| 10/28/03 1119 | X17 (1110) | 30.1 | 1.82 | 1.0 |
| 10/29/03 2120 | X10 (2049) | 7.1 | 1.24 | 4.2 |
| 11/02/03 1738 | X8.3 (1725) | 13.4 | 1.23 | 3.5 |
| 11/03/03 0950 | X3.9 (0955) | 2.7 | 1.40 | 1.9 |
| 11/04/03 1950 | X28 (1948) | 52.7 | 1.50 | 2.1 |
| 7/15/04 0208 | X1.8 (0141) | 2.7 | 1.13 | 19.2 |
| 7/16/04 0225 | X1.3 (0206) | 3.8 | 1.18 | 16.2 |
| 7/22/04 0053 | M9.1 (0032) | 3.5 | 1.24 | 5.1 |

[a]The EUV Norm Factor is the normalization in the 40–100 nm range to the X17 flare on 28 October 2003 and is used for Figure 7.

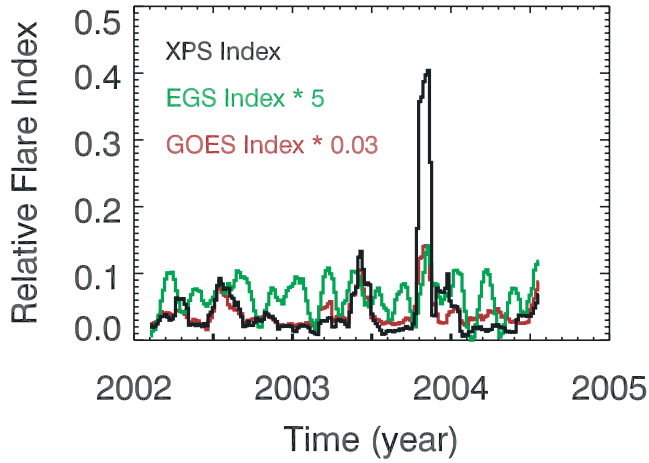


**Figure 5.** Time series of the XUV Photometer System (XPS) (0.1–7 nm), EGS (EUV), and GOES (0.1–0.8 nm) flare indices. These relative flare indices are the ratio of the flare irradiance to the minimum irradiance of the day and then minus unity. Furthermore, the time series plotted is from the running mean of 30 days of data, and the EGS and GOES indices are scaled to be similar as the XPS index. The three most intense flare periods are July 2002, June 2003, and October 2003.

at 49.9 nm and 52.1 nm (log $T = 6.23$), the O VI emission at 103.8 nm (5.42), the C IV emission at 154.9 nm (5.00), the Si IV emission at 140.3 nm (4.75), the N II emission at 108.5 nm (4.40), and the He I emission at 58.4 nm (4.25).

[65] Time series of the XPS and EGS indices differ from the GOES index because different wavelengths are used and because SEE has only a 3% duty cycle as compared with the GOES 100% duty cycle. Compared with the GOES index in Figure 5 are the SEE flare indices minus unity; thus a value of zero represents a quiet period. Temporal variations are similar, overall, with the largest difference being the October 2003 period, whose difference is caused by the SEE observations including the peak measurements of both the X17 and X28 flares. These time series of flare indices indicate four interesting periods for studying flares during the TIMED prime mission: April 2002, July 2002, June 2003, and October 2003. The most recent storm period in July 2004 is also similar in magnitude as the June 2003 period.

[66] Comparisons of the flare indices to each other also clarify some of the differences in the flare time series. The comparison of the XPS relative flare index to the EGS and GOES indices is given in Figure 6. The XPS and GOES flare indices are well correlated as shown in the bottom panel of Figure 6. This result is expected because both are derived from XUV irradiances, 0.1–7 nm for XPS and 0.1–0.8 nm for GOES. However, their relationship is not a linear one but is instead better fit as a power law as given in Figure 6. The EGS and XPS flare indices are not well correlated, and thus differences in the flare time series are expected. The EGS flare is derived from EUV emissions that are known to be sensitive to the position of the flare on the solar disk. The EUV emissions from a flare are brighter when the flares are near disk center due to the optical thickness of most of the EUV emissions [*Donnelly et al.*,

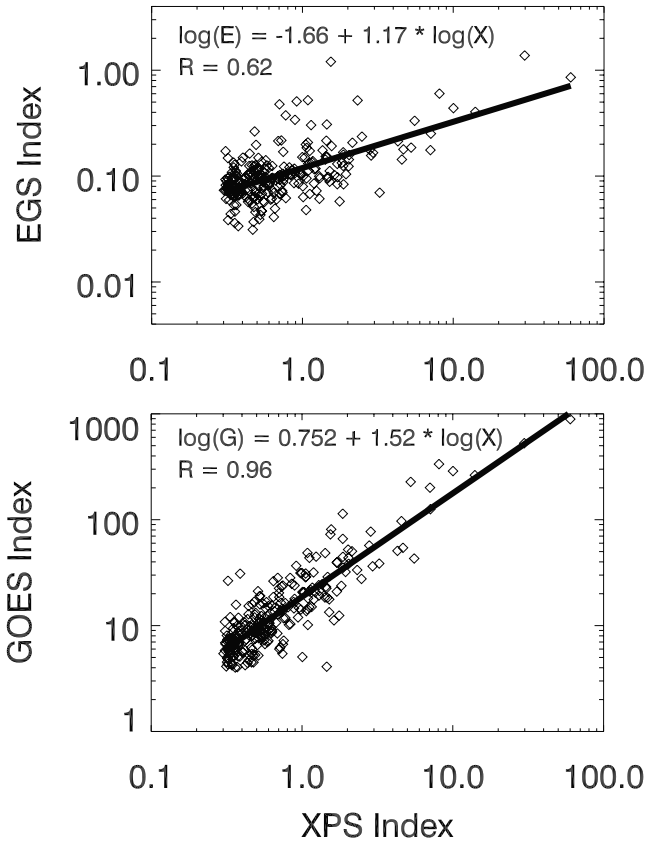


**Figure 6.** Comparison of flare indices. The XPS flare index is compared to the EGS and GOES flare indices. These indices are the relative flare indices that have unity subtracted from the ratio of the flare irradiance to the minimum irradiance of the day. The XPS index is well correlated with the GOES index, being that both are derived from soft X-ray emissions. The EGS index is derived from EUV emissions that are more sensitive to flare position on the solar disk; therefore the correlation ($R$) with the EGS index is moderate.

1976], whereas the XUV emissions are more optically thin and are less sensitive to flare location on the solar disk.

[67] A comparison of the flares on 28 October 2003 and 4 November 2003 illustrate these differences as the XPS 0.1–7 nm irradiance increased by factors of 34 and 57, respectively. These factors are consistent with the GOES X-ray classification of X17 and X28 for these two flares even though the X17 flare occurred near disk center and the X28 flare was from the solar limb. On the other hand, the EUV irradiance changed by a factor of 2 and 1.5 for the X17 and X28 flares, respectively. That is, the EUV irradiance as measured at Earth from the X28 flare is less than the irradiance from the X17 flare and is due to the X28 flare being on the limb. Because of the EUV irradiance sensitivity to flare position, the distribution of the EGS flare index to the XPS flare index is not expected to be a linear or power law relation. The data that are to the left and above of the fit in Figure 6 (top) are most likely from the flares near disk center, and the data to the right and below are from flares near the limb. In addition, there are sometimes EUV enhancements from flares with little X ray enhancements (R. Viereck, private communication, 2004), so the EGS flare index is again expected to be spread more to the left and above the fit as shown in Figure 6. Because of these differences for XUV and EUV irradiance changes for flares, the EGS and XPS flare indices are not well correlated.

[68] The April 2002 and October 2003 solar storm periods during the TIMED mission have received much attention. *Woods et al.* [2003] give a detailed analysis of the 21 April 2002 flare event and include comparisons to the modeled solar EUV irradiance during the Bastille Day 2000 flare [*Meier et al.*, 2002] and modeling of the photoelectron flux changes instigated by this flare event. As additional flare information, *Woods et al.* [2004b] give total and spectral solar irradiance results from SORCE and TIMED for the 28 October 2003 flare.

[69] The ratio of the flare irradiance spectrum to the preflare spectrum clarifies spectral feature increases during the flare event. These ratios for the large X-class flares listed in Table 4 indicate more than a factor of 50 increase in the X-ray region measured by XPS compared with less than a factor of 2 increase for the EUV region measured by EGS. The average variability for these flares is shown in Figure 7 as the ratio of the irradiance near flare peak to the preflare irradiance minus one. The flare variations are normalized to the X17 flare variations between 40 and 100 nm, as listed in Table 4, before taking the average. The EGS flare spectra show much weaker variations than the X-ray variations, as expected, and shows that the variations are generally uniform throughout the EUV spectral region, rather than dominated by coronal emissions, an unexpected result. It appears that these flares had little, if any, effect on increasing the solar irradiance above 180 nm. The normalized variations are fairly similar between the different flares, but significant differences do exist, probably because the SEE flare measurements are at different phases of a flare event. A detailed study of the 200 flare observations by SEE prom-

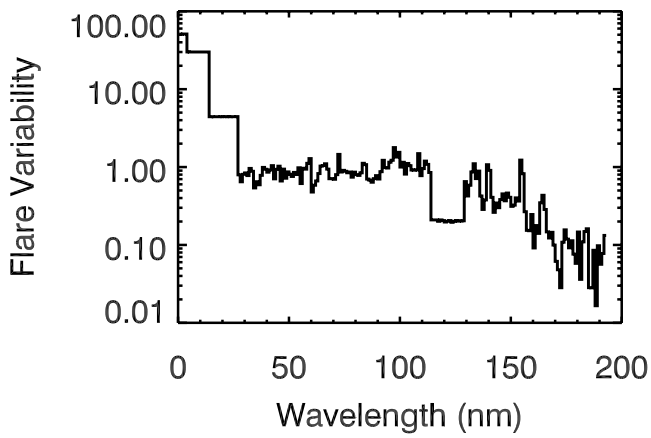


**Figure 7.** Average spectral variation for the large flares listed in Table 4. The flare variation is defined as the flare spectrum divided by the pre-flare spectrum and minus one. All the flares are normalized to the X17 flare variability between 40 and 100 nm before taking the average. The dip near 120 nm is only the measure of the H I Lyman-$\alpha$ variability because the range from 114 nm to 128 nm is derived using a model spectrum scaled to the Lyman-$\alpha$ variability measured by EGS.

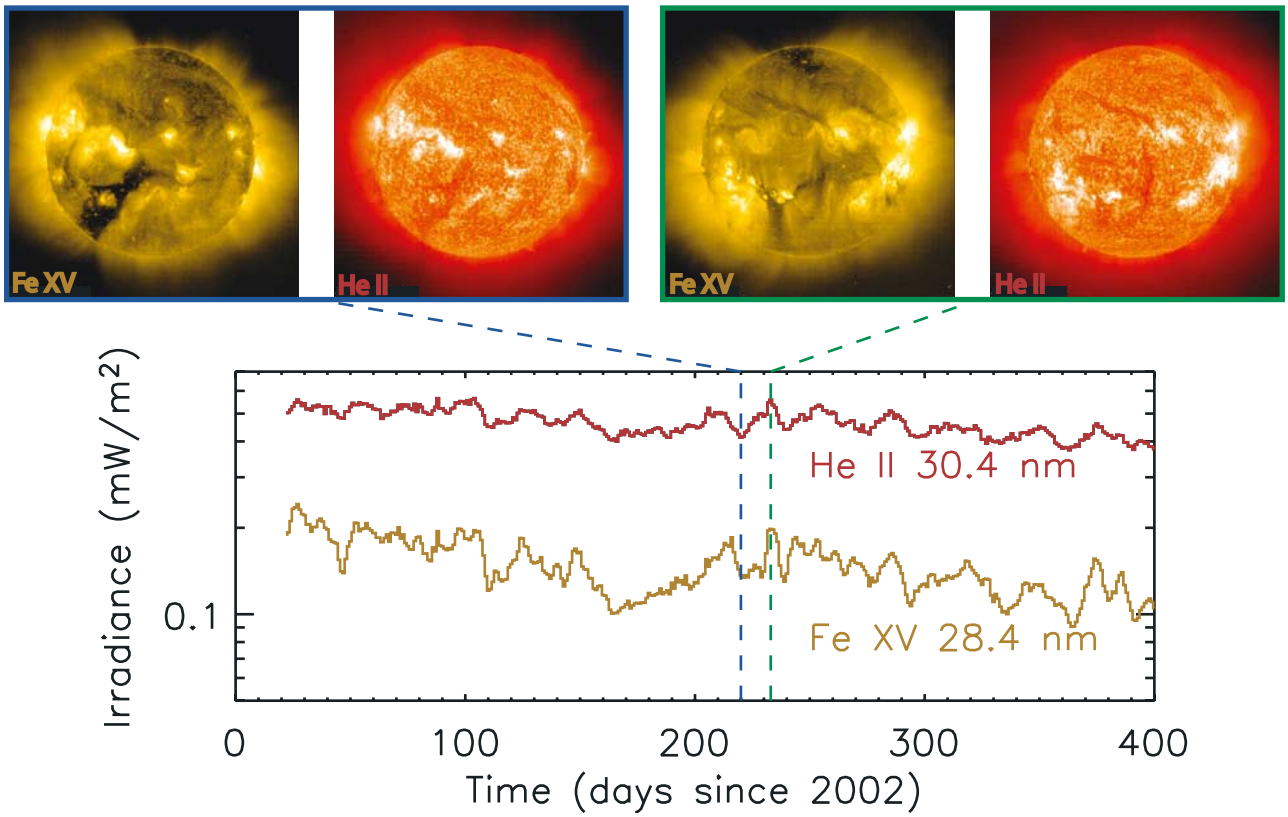


**Figure 8.** The solar irradiance measurements from SEE are shown for the transition region He II 30.4 nm emission and the coronal Fe XV 28.4 nm emission. The primary variations seen in these data are caused by the rotation (~27 days) of the active regions on the Sun. The SOHO EIT images for those emissions are shown above for a particularly strong solar rotational variation in August 2002.

ises new insight on the time profiles of flares as a function of wavelength.

### 5.2. Solar Rotation Variations

[70] One of the dominant variations observed in the solar irradiance time series is due to the solar rotation. These variations are mainly observed with a period near 27 days, which is the mean rotation rate of the Sun. Because of differential rotation (equator rotating faster than poles) and the inhomogeneous distribution of active regions on the Sun, solar rotation variations actually range in period from 25 to 30 days. In addition, there are epochs when the distribution of active regions on opposite sides of the solar hemisphere produces a strong variation of about 13.5 days (half the solar rotation period) with amplitude reduced below the 27-day variations. These 13.5-days variations depend on the center-to-limb variation of each emission and thus have a strong wavelength dependence that can differ from the 27-days variations [*Donnelly and Puga*, 1990; *Crane et al.*, 2004].

[71] August 2002 provides an example of a particularly strong solar rotation variation observed by SEE. The time series of the transition region He II 30.4 nm emission and the coronal Fe XV 28.4 nm emission are shown in Figure 8. While these two emissions have similar variations, each emission is uniquely different due to the different processes in the different layers of the solar atmosphere. For example, the effect of coronal holes is more obvious in the Fe XV emission, while that of the active network is more pronounced for the He II emission. The SOHO EIT images at those wavelengths are also shown in this figure for the dates of 2002/220 (8 August) and 2002/233 (21 August). Because this period is near solar maximum, there are several active regions on the solar disk even during the valley of a solar rotation.

[72] The ratio of the spectrum on 2002/233 to that on 2002/220 gives the spectral variations for this solar rotation and is shown in Figure 9. These variations are compared in the FUV to the model of the solar FUV irradiance that is based on the UARS SOLSTICE measurements [e.g., *Woods and Rottman*, 2002]. The excellent agreement for this FUV comparison indicate that the SEE measurements have comparable relative accuracy to the UARS measurements.

[73] Spectral analysis of the SEE time series provides additional insight into the solar rotation variations. One simple analysis characterizes the variance in the frequency domain using a Fast Fourier Transform (FFT) of the time series from 2002/039 to 2004/039. The ending date was chosen to exclude the enhanced variations in the EGS data that are related to extreme, local degradation of the EGS detector at the bright emission features. While the solar count rates at these bright emissions are still high (well above the dark level), the flat-field calibration count rates are low and adversely affect the Version 7 data set at some wavelengths. An improved flat-field calibration algorithm is

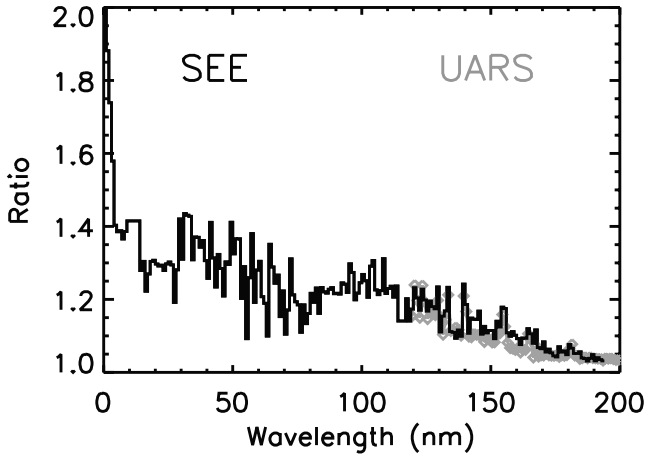


**Figure 9.** The ratio of the SEE spectrum on 2002/233 (21 August) to that on 2002/220 (8 August) is shown as the black line. The line with diamonds (gray) is the FUV variation predicted by a model based on the UARS SOLSTICE measurements.

planned for SEE Version 8 data processing to correct this known effect in the EGS time series.

[74] Spectral density power at 121.5 nm (H I Lyman-$\alpha$) and 170.5 nm are shown in Figure 10. The variations near 13.5 days and 27 days are the dominant periods for most wavelengths. The TIMED orbit precession is about 70 days, and orbit variations are evident in the power spectra, primarily for the EGS data longward of 27 nm and most evident longward of 150 nm where the solar variability is intrinsically small. Changes of the instrument FOV response and gain changes of the detector with temperature are examples of responsivity changes related to satellite orbit variations. While corrections for FOV and temperature changes are applied in creating the SEE Version 7 data products, these corrections are only accurate to a couple percent. Refined, or possibly new, orbit-related corrections could improve the future SEE data products.

[75] The FFT analysis of the SEE Level 3 time series in 2002–2004 quantifies the solar rotation variations near 13.5 days and 27 days. The few time gaps in the SEE data (see Table 2) are filled using interpolation between nearby days. As shown in the examples in Figure 10, the FFT results at 11–16 days and 22–32 days are summed to represent the 13.5 days and 27 days variations, respectively. The background (continuum) is removed from the power spectrum before doing this summation. These variations, which are manifested by solar rotation, are shown in

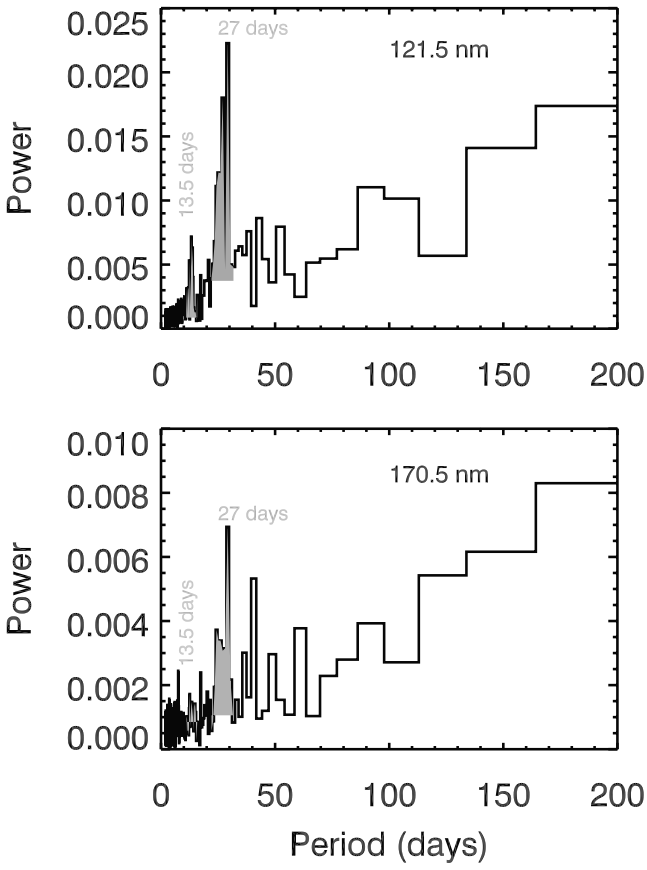


**Figure 10.** Spectral analysis results for the 2002–2004 time period are shown in the top and bottom panels at 121.5 and 170.5 nm, respectively. The results for 13.5-day and 27-day variations are highlighted in each panel.

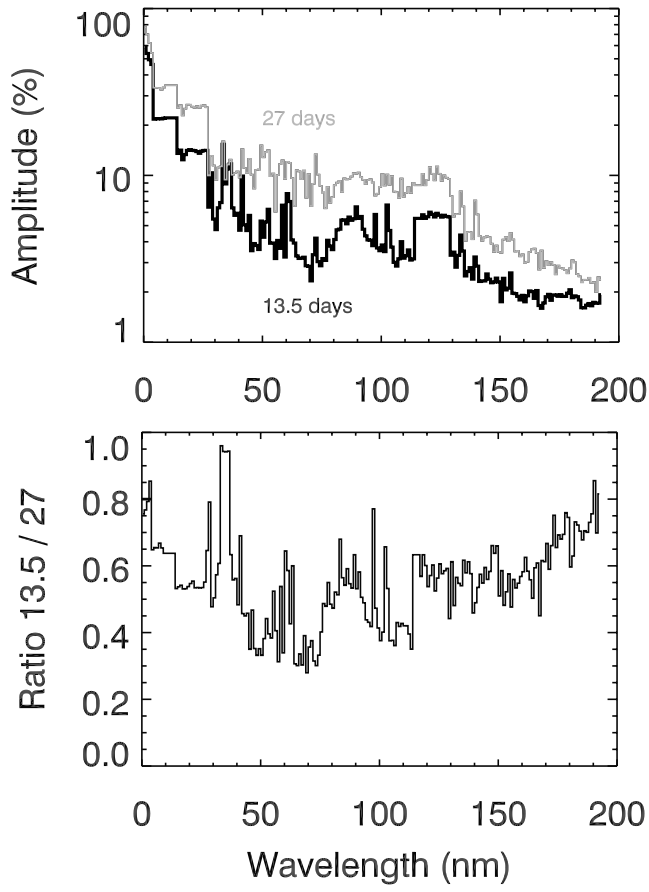


**Figure 11.** Solar variability at 13.5 days and 27 days is shown for the 2002–2004 time period. The 13.5 days variability relative to the 27 days variability, depicted as the ratio in the bottom panel, is larger for emissions that have large limb brightening, such as for coronal emissions, and for emissions that have large limb darkening, such as between 168 nm and 210 nm [*Crane et al.*, 2004].

Figure 11. The FFT analysis using a 200-day sliding window indicates that the 27-day variation peaks in March 2003 and again in late 2003 and that the 13.5-day variations are elevated throughout 2003. The 13.5-day periodicity is most clearly seen in the SEE time series in mid-2003; for example, there are time series of a few emissions shown in Figure 13 in the next section. As expected, the 13.5-day variations are less than the 27-day variations.

[76] As stated earlier, the 13.5-days variations depend on the center-to-limb variation [*Donnelly and Puga*, 1990; *Crane et al.*, 2004], thus the ratio of the 13.5-days variability to the 27-days variability varies strongly with wavelength, as shown in Figure 11. These results reconfirm that the 13.5-days variations longward of 170 nm are larger than the FUV results shortward of 170 nm as explained by *Crane et al.* [2004] in modeling the UARS SUSIM variations. *Crane et al.* [2004] show that the FUV wavelengths with the largest limb darkening, namely in the 168 nm to 210 nm range, have the largest 13.5-day variations as compared with the other FUV wavelengths that have slight limb brightening. The peak irradiances for these limb darken wavelengths occur when two dominant active regions that are ~180° apart are near disk center. An important result from the SEE analysis is that the coronal emissions, such as the Fe XVI 33.5 nm and Mg IX 36.8 nm emissions, also have strong 13.5-day variations. The peak irradiances for coronal emissions, which typically have large limb brightening, occur when two dominant active regions that are ~180° apart are near the limbs and thus are expected to be out of phase with the FUV 13.5-day variations by a few days.

[77] Indeed, the TIMED SEE data support this concept of phase shifts of the coronal emissions relative to other UV wavelengths, and the 13.5-day variations in mid-2003 clearly demonstrate this result. Figure 12 shows the daily time series of four emissions in the top panel for mid-2003 and the phase shift as a function of wavelength relative to the NOAA Mg II C/W index in the bottom panel. The four emissions in this figure are the 33–37 nm irradiance that is mostly coronal emissions, the 30.5 nm irradiance that is the combination of the transition region He II 30.38 nm emission and the coronal Si XI 30.33 nm emission, the 121.5 nm irradiance that is the upper chromospheric and transition region H I 121.6 nm emission, and the NOAA Mg II C/W index that represents the lower chromosphere. The phase shift algorithm is a simple search for the peak irradiance at each wavelength within a 19-day period centered on the peak of the Mg II C/W index. Two examples of the phase shift results are shown in the bottom panel. The phase shift result for day 2003/091 represents a typical interval when the 27-day periodicity is dominant, and the result for day 2003/186 represents a typical interval when the 13.5-day periodicity is dominant. For this 27-day periodicity interval, the phase shifts relative to the Mg index are near zero with a typical shift of 1–2 days. Considering the day-to-day noise in the SEE measurements, the uncertainty of the phase shift is about 1 day. For this 13.5-day periodicity interval, the phase shifts have an offset of +4 days for most FUV wavelengths while the EUV wavelengths have phase shifts ranging from −6 days to +9 days. Many of the wavelengths with the larger phase shifts are from coronal emissions, and their peaks are occurring when the primary active regions are near the limb.

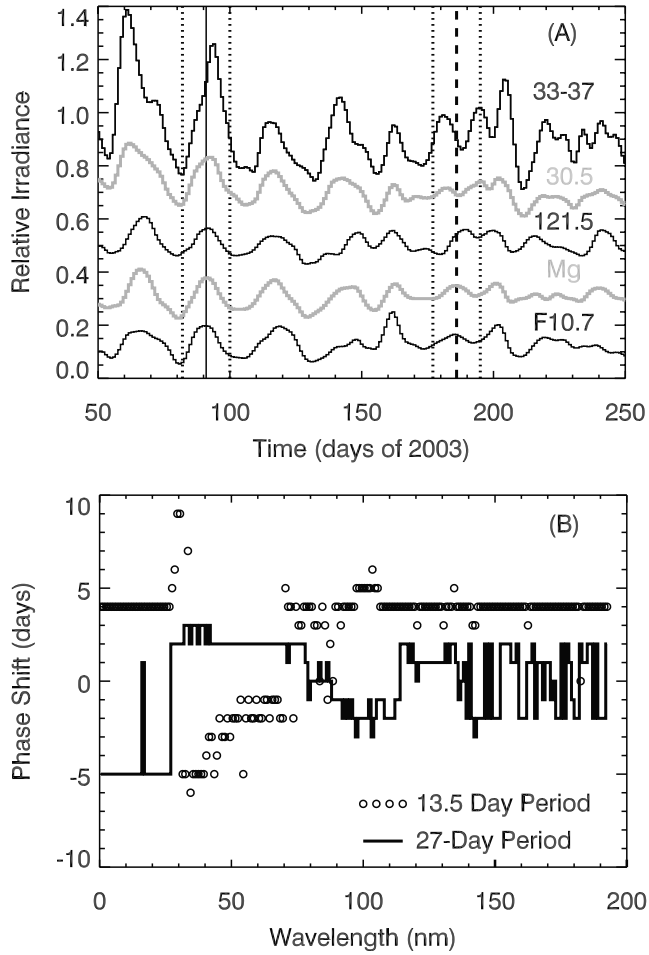


**Figure 12.** (a) The time series of the irradiances at 33–37 nm, 30.5 nm, and 121.5 nm, the NOAA Mg II index, and the 10.7 cm radio flux ($F_{10.7}$). The Mg II peaks during the 27-day and 13.5-day periodicity times are indicated as the solid and dashed lines, respectively, and the dotted lines in the top panel indicate the range in searching for the peaks at the other wavelengths. (b) Phase shifts for the 27-day periodicity near day 2003/091 and for the 13.5-day periodicity near day 2003/186 are shown as a function of wavelength and are relative to the peak in the Mg II C/W index.

For example, the irradiance at 33–37 nm has two peaks at about ±7 days from the Mg peak at day 2003/186 as shown in the top panel of Figure 12. This result is the expected response for emissions with large limb brightening. Neither the Mg C/W index nor the 10.7 cm radio flux ($F_{10.7}$) can predict the observed phase shifts in this example. Examination of other intervals with strong 13.5-day periodicity, such as early and mid-2004, also confirms these results.

[78] Discussions and comparisons of models of the solar UV irradiance follow later in section 7, but a brief comment is warranted here concerning how these phase shift results affect the capability to accurately model the solar UV spectral irradiance. The effect of the phase shifts is primarily important for the EUV wavelengths and for intervals when 13.5-day periodicity dominates. For the more simple proxy modeling approach, these results indicate that multiple

proxies are required to adequately describe the intermediate-term variations over periods of days. A more detailed study is warranted, but at least three different proxies are needed to properly describe the intermediate-term variations in the corona, transition region, and chromosphere. Many of the proxy models (see section 7) use a single proxy, and these models are capable of predicting the long-term variations over periods of months to years but will be less accurate for the intermediate-term variations at many EUV wavelengths. The more physical based models that analyze solar images for active regions and network features and then apply wavelength specific radiative transfer (e.g., center to limb variations) should be able to predict these different phase shifts throughout the UV range during the intermediate-term variations.

### 5.3. Solar Cycle Variations

[79] The TIMED mission began with solar maximum conditions in early 2002, and the solar activity has decreased to moderate levels in early 2003 and in 2004. Solar maximum levels appeared again in June 2003 and October 2003 with a series of solar storms. Some emissions from the chromosphere, transition region, and corona are shown in Figure 13 to illustrate the long-term solar variability during the TIMED mission. The lower chromospheric emissions, such as the O I emission, have varied by 20–40% between 2002 and 2004. The upper chromospheric and transition region emissions, such as the H I and He II emissions, vary more by 60–120%, and the coronal emissions, such as the Fe XVI and XUV 0.1–7 nm emissions, vary the most by more than a factor of 4. The 10.7 cm radio flux ($F_{10.7}$), which is sometimes used as a proxy for solar EUV variations, is also shown in Figure 13, and the $F_{10.7}$ variation is 230%. The variations during the 11-year solar cycle are expected to increase as the TIMED mission continues during a period of declining solar activity, to encompass the full range of the solar cycle 23 variability.

[80] The analysis of a 2-year period from solar maximum conditions in February 2002 to moderate levels in February 2004 provides a preliminary examination of long-term

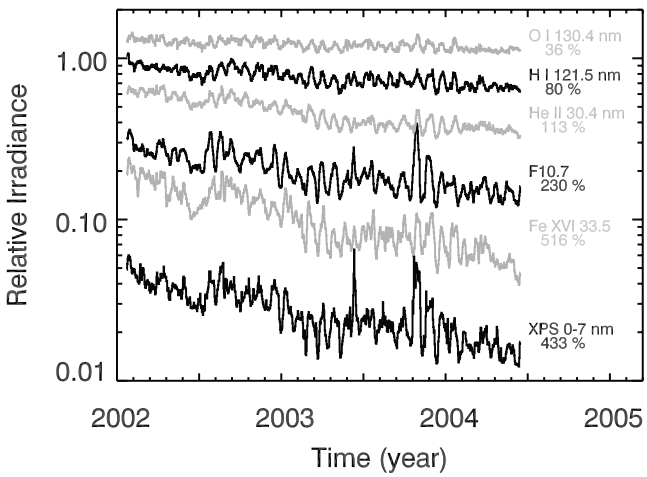


**Figure 13.** Time series of several emissions during the TIMED mission. The emissions are arranged with chromospheric emissions near the top and coronal emissions near the bottom.

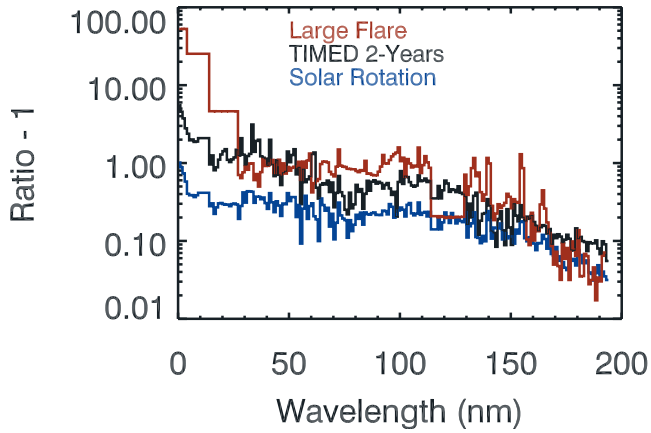


**Figure 14.** Comparison of the variation over the TIMED 2-year mission (black) to flare (red) and solar rotation (blue) variations shows similarity in wavelength.

variations of the SEE observations. These variations shown in Figure 14 represent primarily solar related changes during the first 2 years of the TIMED mission but could also include instrument degradation effects that might not be fully removed in the SEE Version 7 data set. The similarity of the spectral dependence of the 2-year variation with the solar rotation variation (also shown in Figure 14) suggests that the responsivity changes are reasonably corrected for in the SEE data. One concern for the SEE long-term trends is the FUV region longward of 160 nm that has large corrections (~20%) for its recovery during the mission. One interesting result of this comparison is that the coronal emissions, such as the Fe XVI 33.5 nm, Mg IX 36.8 nm, and Mg X 61.0 nm emissions, indicate larger variations during this 2-year period than would be suggested by either the solar rotation or flare variations.

[81] The long-term (solar cycle) variations are expected to be a factor of 2–6 times more than the 27-day solar rotation variations [*Woods and Rottman*, 2002]. However, the long-term variations cannot simply be scaled from the short-term variations using a solar proxy as learned from the UARS measurements [*Woods et al.*, 2000a]. The relative differences between short-term and long-term variations are due to the differences in how the radiation at different wavelengths is manifested in the solar atmosphere. For example, the ratio of the solar cycle variation to the rotation variation for the H I Lyman-$\alpha$ emission is about a factor of 2 larger than the same ratio for the Mg II core-to-wing ratio (Mg proxy). Using results from analyzing solar images, *Woods et al.* [2000a] explained this difference as the result of the differences between the plages and the active network regions on the Sun for different emissions. The active network regions have higher contrast for upper chromospheric and transition region emissions, such as the H I Lyman-$\alpha$ emission, than for lower chromospheric emissions, such as the Mg proxy. Because the active network regions contribute more to the long-term variations than to the solar rotation variations [*Worden et al.*, 1998, 1999], the upper chromospheric and transition region emissions have different long-term behavior than the lower chromospheric emissions. Just as the multiyear UARS mission has led to better understanding of the solar UV irradiance at the longer

wavelengths, an extended TIMED mission will enable significant advances in understanding the long-term variations of the solar EUV irradiance.

## 6. Comparisons With Other Measurements

[82] The Upper Atmosphere Research Satellite (UARS) solar FUV irradiance measurements provide validation for the SEE FUV measurements as both data sets include daily calibrated spectral measurements of the solar FUV irradiance in the 119–194 nm range with 1 nm spectral resolution. The validation of the SEE EUV measurements below 119 nm is more limited because the primary overlapping observations of solar EUV irradiance, made by the Student Nitric Oxide Explorer (SNOE) and the Solar and Heliospheric Observatory (SOHO), have limited spectral coverage. The following sections describe these comparisons.

### 6.1. SNOE Comparison

[83] The SNOE Solar X ray Photometers (SXP) [*Bailey et al.*, 2000, 2001] are very similar to the photometers used in the SEE XPS. Most comparable are the SXP 0.1–7 nm and 17–20 nm irradiance measurements with the 0.1–7 nm and 17–21 nm XPS photometer measurements. Unfortunately, the SNOE SXP measurements only overlap for a few months with the TIMED mission before the SNOE satellite orientation was changed to optimize the NO measurements at the sacrifice of the solar measurements.

[84] An initial comparison of the SEE XPS and SNOE SXP measurements in 2002 showed good agreement when both data reduction schemes used the same solar model [*Hinteregger et al.*, 1981]. This model, referred here as the EUV81 model, is also known as SERF-1 by the Solar Electromagnetic Radiation Flux (SERF) subgroup of the World Ionosphere-Thermosphere Study. These initial comparisons indicated SNOE 0.1–7 nm irradiances about 30% higher than SEE irradiances, and SNOE 17–20 nm irradiances within 5% of SEE. These differences are within the reported calibration uncertainties, which are derived for the SNOE SXP photodiodes calibrations from the NIST SURF-II facility and the SEE XPS photodiodes calibrations from the PTB BESSY facility.

[85] Following discrepancies revealed in the initial analysis of SEE's flare measurements as discussed at the end of section 4.2, the SEE XPS data processing was revised to use responsivity parameters derived with improved solar irradiance models [*Woods and Rottman*, 2002; *Meier et al.*, 2002]. These improved models have irradiance values shortward of 1.8 nm, whereas the EUV81 model has none. Because the Si photodiodes used in SNOE and SEE have maximum responsivity at the very shortest wavelengths, the EUV81 model is inappropriate for analysis of data from Si photodiodes. Changing the solar model used in data processing makes the SEE XPS flare measurements from different photometers consistent with each other, which indicates that the major increase of the solar irradiance during the flare is below 4 nm.

[86] The differences in the derived irradiances from the improved models and that from the EUV81 model are small for the 0–10 nm channels, but the irradiances derived from the improved models are significantly reduced by a factor of 1.5–3.7 for the other channels between 10 and 34 nm. More specifically, the improved models changed the balance of the $f_{E\_total}$ parameter in equation (4) between the short XUV bandpass and the long XUV bandpass than what was originally derived using the EUV81 model. The XPS responsivities, $R$, for the different models are listed in Table 5 for three photometers, and the resulting irradiance will be lower when the responsivity is higher. These results indicate that the EUV81 model introduces large systematic errors for channels with bandpasses at the longer XUV wavelengths. The VUV2002 model has 1 nm resolution and causes offsets for the derived responsivities related to its low resolution. The EUV81 and NRLEUV models are both provided at 0.1 nm resolution, and the NRLEUV model results for the responsivities are used in Version 7 XPS processing. This comparison emphasizes one of the challenges in analyzing broadband measurements in the XUV range in that the results can be model dependent. These differences also indicate that the irradiances from the XUV photometers in the 10–34 nm range have much larger model uncertainties than the calibration uncertainties. The most accurate measurements from the XUV photometers are from the 0.1–10 nm channels because the measured currents directly reflect the total energy in its broadband and do not require a correction for the short wavelength contribution to the total current.

**Table 5.** XPS Responsivity Changes Using Different Solar Models[a]

| Solar Model | XP#1 0.1–7 nm | XP#5 0.1–10 nm | XP#7 17–21 nm |
|---|---|---|---|
| EUV81$\langle T\rangle$ | 0.120 | 0.122 | 0.0435 |
| $f$ | 1.053 | 1.014 | 1.352 |
| $R = f \bullet \langle T\rangle$ | 0.126 | 0.124 | 0.0588 |
| NRLEUV$\langle T\rangle$ | 0.124 | 0.143 | 0.0425 |
| $f$ | 1.015 | 1.005 | 3.445 |
| $R = f \bullet \langle T\rangle$ | 0.126 | 0.144 | 0.146 |
| $R/R$(EUV81) | 1.00 | 1.16 | 2.46 |
| VUV2002$\langle T\rangle$ | 0.172 | 0.172 | 0.0402 |
| $f$ | 1.019 | 1.030 | 2.644 |
| $R = f \bullet \langle T\rangle$ | 0.175 | 0.177 | 0.106 |
| $R/R$(EUV81) | 1.39 | 1.43 | 1.81 |

[a]The weighted transmission, $\langle T\rangle$, and the fraction of bandpass, $f$, are listed for three of the XUV Photometers (XP). The irradiance is inversely proportion to the responsivity product of $f \bullet \langle T\rangle$. The solar models are the EUV81 [*Hinteregger et al.*, 1981], NRLEUV [*Meier et al.*, 2002], and VUV2002 models [*Woods and Rottman*, 2002].

[87] In addition, the SEE Version 7 data processing has been updated with the calibration rocket results, which include an updated NIST SURF-III calibration for the rocket XPS using improved techniques. The SEE XPS photodiodes were calibrated at PTB/BESSY in the 0.8 to 25 nm range, but these responsivity results have differences with calibrations done at NIST/SURF-III in the 5 to 30 nm range for some of the same photodiodes by as much as a factor of 2 at wavelengths between 5 and 12 nm. Both of these calibrations are performed with a monochromator and reference photodiode, and both have corrections to the derived responsivity for the monochromator's scattered light and higher-order grating contributions. To help understand these differences, the rocket XPS was calibrated directly viewing the SURF synchrotron source using multiple beam energies to derive the responsivity without a monochromator. These rocket XPS responsivity results agree best with the PTB/BESSY results shortward of 5 nm and at 17–22 nm and agree well with all of the SURF monochromator results.

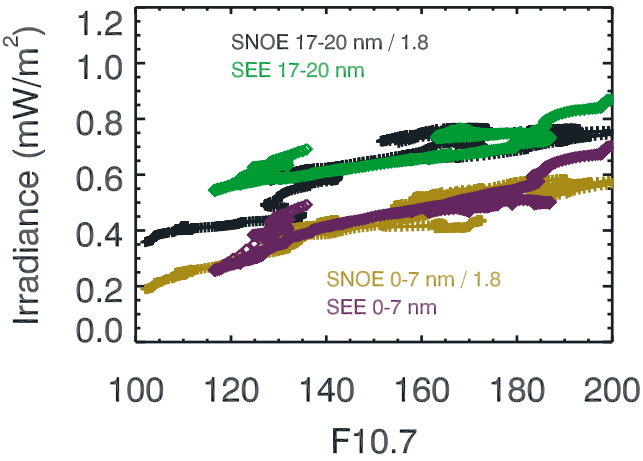


**Figure 15.** Comparisons of the SNOE and SEE XPS measurements show differences in magnitude and with solar activity. The comparison of the SNOE 17–20 nm (black plus symbols) indicates a factor of 1.8 difference, and the comparison of the SNOE 0.1–7 nm (orange plus symbols) indicates a factor of 1.8 difference. The differences with solar activity are related to flare periods, such as October 2003, that do not correlate well with $F_{10.7}$.

These new rocket XPS calibrations have been transferred to the SEE XPS and have made significant differences for the responsivities by about a factor of 1.4 for most photometers. As a consequence of the new calibration and different solar model in the processing algorithm, the SEE Version 7 irradiances in the 0–27 nm range are lower by about a factor of 2 for most photometers as compared to the SEE Version 6 results.

[88] In the new comparisons of the SEE Version 7 results and recently revised SNOE SXP measurements as shown in Figure 15, both the SNOE 0.1–7 and 17–20 nm irradiances are a factor of 1.8 higher than the SEE values. The suggestion that the solar XUV irradiance is a factor of ~4 more than the EUV81 model predictions [*Bailey et al.*, 2000; *Solomon et al.*, 2001] is revised to a factor of ~2 from the new TIMED SEE results. This result has implications for photoelectron production and corresponding effects on airglow emissions such as the FUV airglow measurements by the TIMED Global Ultraviolet Imager (GUVI). *Strickland et al.* [2004] report that the GUVI airglow results support the EUV81 model predictions without any scaling factor shortward of 20 nm. On the other hand, another analysis of the GUVI airglow data indicates that the GUVI data are consistent with a scale factor of 2 shortward of 20 nm for the EUV81 model predictions (D. Morrison, private communication, 2004). While the differences are now reduced between the solar EUV irradiance measurements and solar irradiance predictions from photoelectron and airglow measurements, additional validation studies are warranted concerning the solar XUV irradiance and/or excitation cross sections that contribute to the photoelectron distribution and airglow emissions.

### 6.2. SOHO Comparison

[89] While there are a few solar EUV measurements made by SOHO, only the Solar EUV Monitor (SEM) provides irradiances on a daily basis and with high accuracy [*Judge et al.*, 1998]. The SEM irradiance results at 26–34 nm (first grating order) and at 0–50 nm (zeroth order) are compared to the SEE Level 3 irradiances integrated over the same wavelength bands. The SEM irradiances are reported in photon units instead of energy units and are derived by scaling a reference spectrum [*Woods*, 1992] to match the SEM photodiode currents. The ratio of this reference spectrum over the desired bandpass in energy units to itself in photon units is used to convert the SEM irradiances to energy units. The comparison of these two measurements, shown in Figure 16, show that SEE results are lower than SEM results by 20% at 26–34 nm and in good agreement at 0–50 nm. The difference at 26–34 nm is within the combined calibration uncertainties. The uncertainty for the SEM measurement is about 10%, and the uncertainty for the SEE 26–34 nm measurement is about 20%.

[90] Once SEM and SEE are scaled to the same level, the comparisons indicate good agreement in their relative temporal variations, which in turn indicate good understanding of instrument degradation functions for both instruments. Both SEE and SEM show an overall 50% reduction in the 26–34 nm irradiance over the 2 years of the TIMED mission. The differences in the time series for the 0–50 nm irradiances might be due to the reference spectra used in the

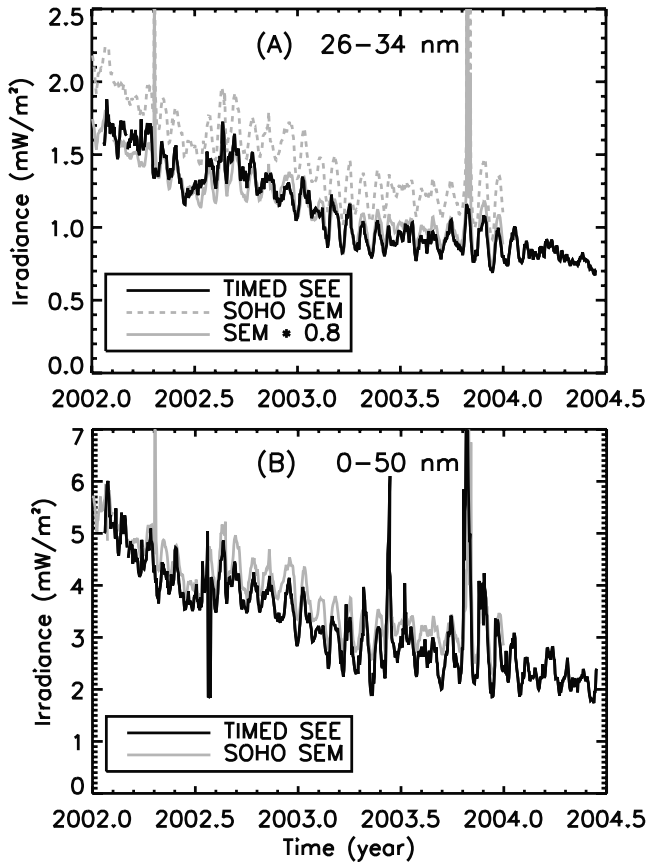


**Figure 16.** The SEE L3 data are compared to the SOHO SEM measurements at 26–34 nm (top) and at 0–50 nm (bottom). The SEE measurements at 0–50 nm are in good agreement with the SEM results, and the SEE measurements at 26–34 nm are 20% lower than the SEM results.

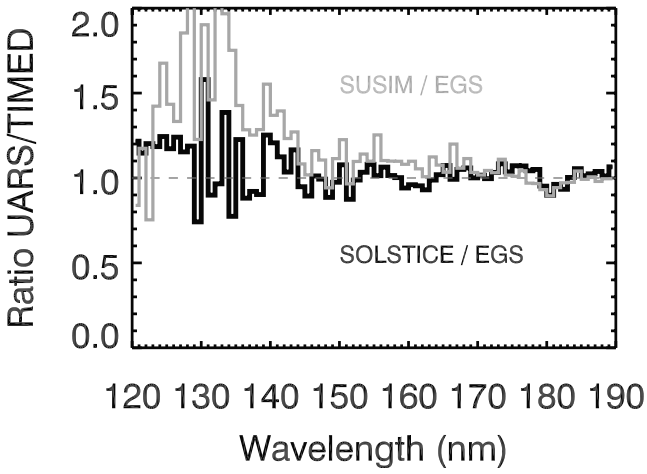


**Figure 17.** The SEE results in the FUV are compared to the UARS measurements on day 2002/039. The SEE and UARS SOLSTICE irradiances agree to within 10% as EGS data processing used UARS SOLSTICE for normalization. The analysis of the rocket measurements on day 2002/039 also confirmed these values to within 20% across the full FUV range. The UARS SUSIM results have differences shortward of 145 nm as expected from previous comparisons of UARS SUSIM and UARS SOLSTICE measurements [*Woods et al.*, 1996].

SEM and SEE XUV data processing. The SEM processing uses a single reference spectrum, and SEE processing uses a daily reference spectrum based on the VUV2002 model [*Woods and Rottman*, 2002]. In both cases, the reference spectra are scaled to match the photodiode currents. Some of these differences might be resolved if SEM and SEE used the same reference spectra. Nonetheless, relative changes in the 0–50 nm irradiances are in good agreement throughout the TIMED mission.

### 6.3. UARS Comparison

[91] The UARS makes two different solar FUV irradiance measurements, one by the Solar Stellar Irradiance Comparison Experiment (SOLSTICE) [*Rottman et al.*, 1993], and another by the Solar Ultraviolet Spectral Irradiance Monitor (SUSIM) [*Brueckner et al.*, 1993]. Both measurements provide similar spectral coverage and resolution, but they use different in-flight calibration techniques. The SOLSTICE uses bright, early-type (O, B) stars for tracking its degradation, and SUSIM uses redundant channels and onboard deuterium lamps. Although both SOLSTICE and SUSIM have daily measurements throughout most of 2002, the majority of these UARS solar irradiance results are not currently available due primarily to delays in the conversion of the original data processing code to new systems. Therefore only a limited comparison is now possible, and a more complete validation awaits the new UARS data sets.

[92] The comparison of the UARS SOLSTICE and SUSIM measurements with those of EGS, as shown in Figure 17 for day 2002/039, indicates good agreement for the absolute values of the FUV irradiance from EGS. The initial comparison of EGS using its preflight calibration indicated good agreement with the largest difference being the EGS 120–140 nm irradiances that are about 10% lower than the UARS SOLSTICE measurement. Since then, the EGS responsivity in the FUV region was adjusted and confirmed by the rocket EGS measurement that was made on day 2002/039. The current differences are relatively small and are within the individual measurement uncertainties with the UARS irradiance uncertainties being 3–7% in the FUV range [*Woods et al.*, 1996]. The largest difference is seen shortward of 145 nm between UARS SUSIM and EGS and SOLSTICE. This difference of ~30% is similar to the comparisons made between UARS SUSIM and SOLSTICE early in the UARS mission [*Woods et al.*, 1996]. The 125–145 nm range is often problematic because of the low signal levels in this range.

[93] The responsivity of the SEE EGS instrument has increased during the TIMED mission. A concept that could explain this recovery behavior is that the resistance of the EGS detector microchannel plates (MCPs) is decreasing with time and thus causing a gain increase of the detector. A resistance change of the MCP is possible as the bright solar lines are significantly degrading the MCPs at the local regions where the bright emissions illuminate the detector. While the redundant, calibration channel of EGS can track in-flight changes between the normal and calibration channels, a uniform change of the EGS detector would also cause uniform changes for both the normal and calibration channels. Therefore external calibrations, such as the SEE calibration rocket experiment and other solar irradiance measurements from UARS and SORCE, are critical to establish the long-term degradation changes for SEE. The SEE rocket calibration measurements on about an annual basis are used exclusively to establish the SEE long-term degradation changes in the XUV and EUV. The daily solar FUV irradiance measurements by UARS SUSIM and SORCE SOLSTICE are used for the degradation analysis of SEE in the FUV, as these daily measurements provide a higher time cadence.

[94] With corrections applied for responsivity changes, the SEE Version 7 data are compared to UARS SUSIM and SORCE SOLSTICE measurements in Figure 18. The offsets in the ratios indicate irradiance shifts resulting from absolute calibration differences. These ratios have a long-term

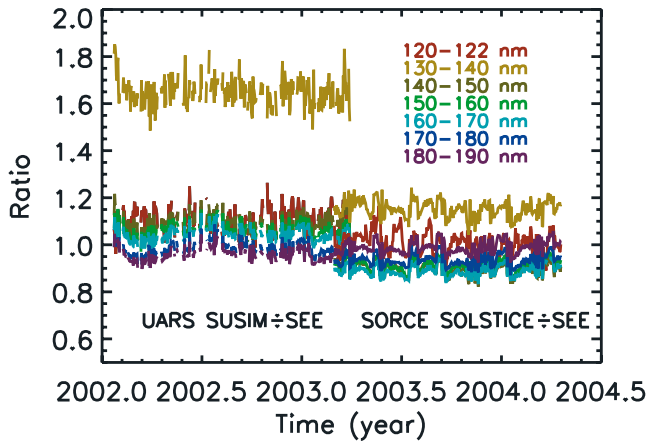


**Figure 18.** The UARS SUSIM and SORCE SOLSTICE measurements are compared with SEE in 10 nm intervals and at Lyman-α. These long-term trends are flat indicating that instrument long-term degradation is properly corrected.

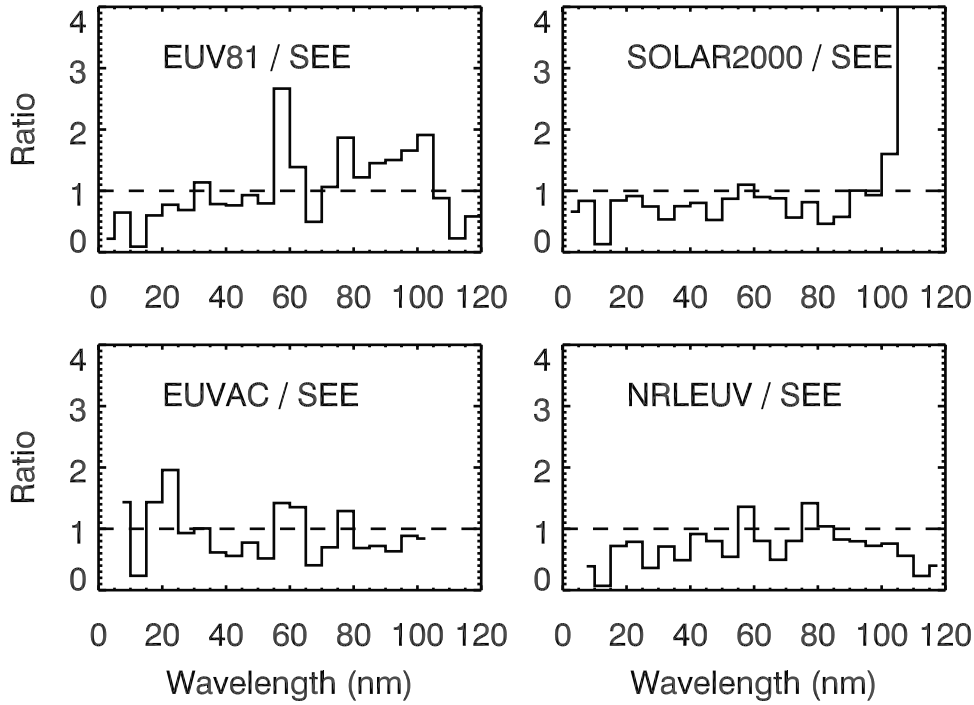


**Figure 19.** The SEE measurement on 8 February 2002 is compared to models of the solar EUV irradiance: EUV81, EUVAC, NRLEUV, and SOLAR2000.

flat trend, indicating that the SEE responsivity changes are properly applied. The two rocket calibration results also confirm this long-term trend. Because the long-term corrections are exponential functions, there are some midterm (months) deviations in these ratios that are not corrected in the SEE data. There are detector temperature gain corrections and field of view corrections that vary with the orbit precession (~70 days). With the precision of these corrections being a few percent, the midterm deviations might partially be related to these orbit-sensitive corrections.

## 7. Comparisons With Models

[95] Because of the limited amount of actual solar irradiance data, especially for the XUV and EUV regions, models of the solar variability are widely used in aeronomic studies. Commonly used solar irradiance models are empirical models, frequently called proxy models, that are derived using linear relations between one or two solar proxies and extant observations of the solar VUV irradiance. These models use readily available solar measurements, such as the ground-based 10.7 cm radio solar flux ($F_{10.7}$) and the NOAA Mg II core-to-wing index (Mg C/W), to represent solar irradiance variations in the VUV spectral range.

[96] *Hinteregger et al.* [1981] developed the first, and still, widely used proxy model based on the AE-E satellite observations and several sounding rocket measurements. The original proxies for this model were the chromospheric H I Lyman-β (102.6 nm) and the coronal Fe XVI (33.5 nm) emissions. As measurements of these emissions are not generally available, they are constructed from correlations with the daily F10.7 and its 81-day average, which have been available on a daily basis since 1947. The *Hinteregger et al.* [1981] model is also referred to as EUV81 and SERF 1 by the Solar Electromagnetic Radiation Flux (SERF) subgroup of the World Ionosphere-Thermosphere Study.

[97] *Richards et al.* [1994] developed a different $F_{10.7}$ proxy model called EUVAC in which the solar soft X-ray irradiances were increased by a factor of 2 to 3 compared with the SERF 1 model. W. K. Tobiska has developed several proxy models of the solar EUV irradiance: SERF 2 by *Tobiska and Barth* [1990], EUV91 by *Tobiska* [1991], EUV97 by *Tobiska and Eparvier* [1998], and the latest version, SOLAR2000, by *Tobiska et al.* [2000]. Augmenting these simple proxy models are physical and semiempirical models of the solar EUV irradiance: *Fontenla et al.* [1999], *Warren et al.* [1998a, 1998b], and *Lean et al.* [1982]. Of these models, the NRLEUV model has been parameterized to use the $F_{10.7}$ and Mg II core-to-wing index as solar proxy inputs [*Warren et al.*, 2001].

[98] An objective of the SEE program is the development of better models of the solar EUV irradiance variability. The comparison of four different solar EUV irradiance models to the SEE measurement on 8 February 2002 (day 2002/039) in Figure 19 at a resolution of 5 nm shows that none of the current models agree well with SEE measurements at all wavelengths. The four models compared in Figure 19 are the EUV81 [*Hinteregger et al.*, 1981], the EUVAC [*Richards et al.*, 1994], the SOLAR2000 version 2.23 [*Tobiska et al.*, 2000], and the NRLEUV [*Warren et al.*, 2001]. The models are typically within 40% of the SEE measurement longward of 30 nm, although there are differences larger than a factor of 2 for a few wavelengths for the EUV81 and SOLAR2000 models. The EUVAC and SOLAR2000 models agree best with SEE shortward of 30 nm, and the EUV81 and NRLEUV models have lower values than SEE shortward of 30 nm.

[99] Another important aspect for model comparisons is the relative variability from day to day and over the solar

cycle. A couple of comparisons are shown here to illustrate some of the issues. The comparisons of the SEE measurements and models of the 5–25 nm and 50–75 nm ranges are shown in Figure 20. Obvious results are that SEE 5–25 nm irradiances are about 70% higher than the EUV81 and NRLEUV values, and EUV81 50–75 nm model estimates are about 50% higher than the SEE and NRLEUV values.

[100] More subtle results are (1) the SEE 5–25 nm irradiances vary more than both model predictions, (2) the SEE irradiances have stronger solar rotation variations than the NRLEUV model predictions, and (3) the SEE 50–75 nm irradiances vary less than the EUV81 model predictions. A possible explanation for the SEE 5–25 nm variations being larger than the models is that the flare effects in the SEE data are not well represented in the $F_{10.7}$ or Mg C/W proxies used by the models. The solar rotation variations from the NRLEUV model are also less than results from the SOHO SEM and SNOE observations [*Lean et al.*, 2003]. The differences between the SEE 50–75 nm measurements and the EUV81 model predictions are likely related to the use of the $F_{10.7}$ proxy in the EUV81 model because the $F_{10.7}$ is not well correlated with the chromospheric and transition region emissions, which dominate the 50–75 nm range.

[101] The SEE measurements are also compared to the UARS proxy model by *Lean et al.* [1997] in selected wavelength bands in Figure 21. The SEE FUV irradiances have very similar absolute values as the UARS proxy model, as expected because the SEE FUV range was calibrated with UARS SOLSTICE measurements in February 2002. The main difference between the SEE FUV irradiances and the UARS proxy model is in the magnitude of the solar rotation variation. This difference is primarily explained for the 170–180 nm comparison because the SEE measurement precision (relative accuracy) is only ~4%. In other words, the SEE daily and long-term variations that can be attributed to observation and calibration effects are expected to be about 4% (the design goal for the SEE instrument) and these instrumental effects are most evident in the long wavelengths of the FUV range where the solar variability is only a few percent. The solar rotation variation difference is primarily explained for the 121–122 nm comparison because the H I Lyman-α irradiance is known to have differences between the long-term and short-term variations relative to the Mg II C/W ratio [*Woods et al.*, 2000a], whereas this UARS proxy model assumes the same long-term and short-term variations between the FUV irradiance and the Mg proxy. More detailed comparisons of the SEE EUV and FUV measurements with the models are warranted.

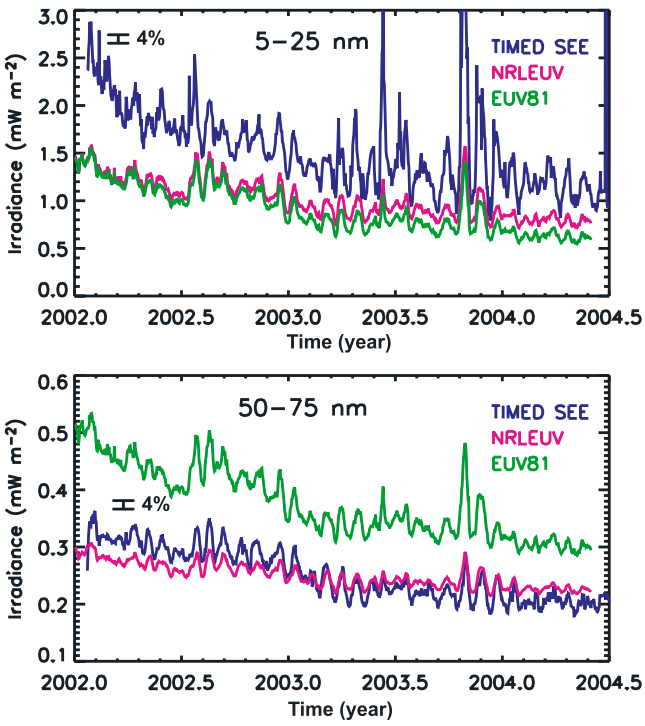


**Figure 20.** The SEE measurements in the 5–25 nm and 50–75 nm ranges are compared with the EUV81 and NRLEUV models. The expected 4% measurement precision of the SEE data is indicated in each plot.

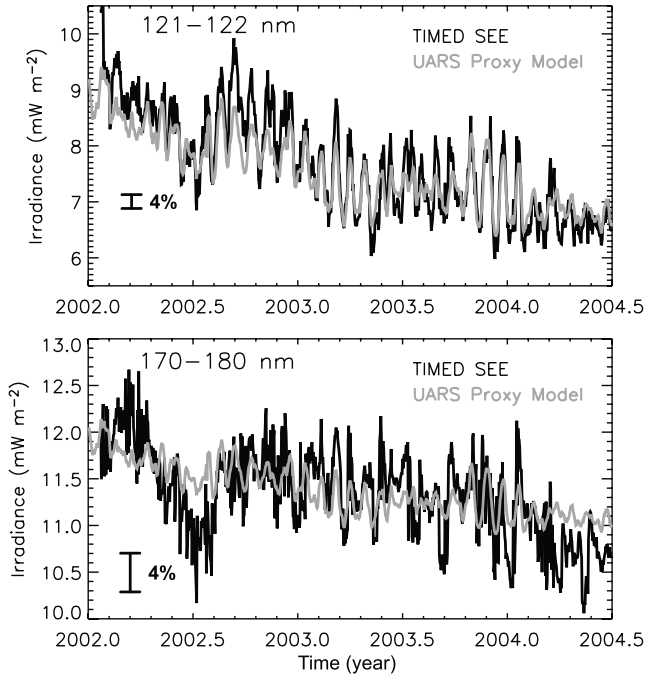


**Figure 21.** The SEE measurements at 121.5 nm and in the 170–180 nm range are compared with the UARS proxy model. The expected 4% measurement precision of the SEE data is indicated in each plot.

[102] With further analysis, the SEE measurements will be used to improve the existing models and to develop new models of the solar EUV irradiance. The solar UV irradiance above 115 nm has been measured more extensively; consequently, models of the solar FUV and MUV irradiance are much more accurate than the solar EUV models, due primarily to the lack of solar EUV measurements during the past two solar cycles. An example of a comparison with a model of the FUV irradiance is included in Figure 9, which is consistent with the SEE results.

## 8. Summary and Future Work

[103] The TIMED SEE instrument is obtaining daily measurements of the solar VUV irradiance with an accuracy of 10–20%. These measurements began on 22 January

2002 and are filling the "EUV Hole," the large gap when there have been limited measurements of the solar EUV irradiance since 1981. Because of rigorous preflight calibrations and the use of different in-flight calibration techniques, the SEE program is providing new information about the solar EUV irradiance, both in the magnitude of the solar irradiance and the amount of the short-term variations caused by flare events and solar rotation of active regions. Continued observations will provide new determinations of solar cycle variability for the EUV range.

[104] In spite of the duty cycle for SEE's solar observations being only 3%, SEE has observed about 200 solar flares during the first 2 years of the TIMED mission. The capability of SEE to measure the full VUV spectrum in 10 s is providing new results on how the solar irradiance changes at all of the VUV wavelengths during a flare event. The variations during the larger flares, such as the X17 flare on 28 October 2003, are as large as the expected solar cycle variations throughout the VUV range.

[105] The SEE measurements also reveal important, new results concerning phase shifts of 2–7 days in the intermediate-term variations between different UV wavelengths. These phase shifts are most evident in the EUV range for coronal emissions and during intervals when 13.5-day periodicity dominates, and this wavelength-dependent effect appears to be related to the center-to-limb variation of each emission. Neither the Mg II C/W index nor the 10.7 cm radio flux can predict the observed phase shifts for the coronal emissions. This effect partially explains why empirical models of the solar UV irradiance with a single proxy are less accurate than empirical models with multiple proxies or physical based models that account for the center-to-limb variations.

[106] The SEE measurements have also validated the solar FUV irradiance and spectral variations due to solar rotation that have been well established by the UARS program. The SEE measurements provide new, more accurate results for the solar EUV and XUV irradiance, addressing both absolute values for the irradiance and temporal variability. The solar EUV irradiances from SEE agree well with the SOHO SEM measurements but indicate differences by more than a factor of 2 at a few wavelengths between the EUV81 and SOLAR2000 models. The solar XUV irradiances from SEE are a factor of 2 lower than the SNOE results but remain higher than the predicted irradiances from the EUV81 and NRLEUV models by more than a factor of 2. While we believe that the SEE measurements are validated at the 10–20% level, it is an on-going task to understand the subtle instrument changes and to improve the irradiance accuracy through better calibrations and improved data processing algorithms.

[107] Additional utilization of the SEE measurements includes modeling the terrestrial response to the solar UV changes, improving models of the solar EUV irradiance, and further validations with other solar measurements. Solar irradiance variations drive many atmospheric processes, such as photochemistry, heating, and dynamics. These solar-terrestrial interactions will be studied using the TIME-GCM [*Roble et al.*, 1988], which is a model of the upper atmosphere that has an option to use the SEE solar irradiance daily measurements as an input. The TIME-GCM results, which can also be compared with other TIMED measurements and ground-based measurements, are expected to provide better understanding of the many coupled processes in the atmosphere. In order to study the atmosphere and support other space weather research, improved models of the solar EUV irradiance are being developed. New understanding of how and why the solar irradiance changes using the SEE measurements and solar images will lead to improvements of the NRLEUV, SOLAR2000, and EUVAC models of the solar EUV irradiance, as well as, possibly lead to development of new models of the solar VUV irradiance. The SEE data will also be valuable for any model development involving flare changes in the EUV range.

[108] Validation of the SEE measurements with independent measurements will also be continued. For example, additional comparisons are planned with the new solar VUV irradiance measurements from the Solar Radiation and Climate Experiment (SORCE) [*Woods et al.*, 2000b]. The SORCE spacecraft was launched on 25 January 2003 and measures the solar irradiance below 34 nm using an XPS like the SEE XPS and the solar irradiance between 115 and 3000 nm using grating and prism spectrometers. If the TIMED mission is extended long enough, then the SEE measurements could overlap with the solar EUV irradiance measurements from the new EUV Sensor (EUVS) aboard the NOAA GOES satellites, the Russian Solar Patrol mission, the ESA Solar Auto-Calibrating EUV/UV Spectrometers (SOL-ACES), and the EUV Variability Experiment (EVE) aboard the NASA Solar Dynamics Observatory (SDO). The GOES EUVS will have five broadband channels centered at 15 nm, 30.4 nm, 60 nm, 90 nm, and 121.6 nm and is expected to be launched in March 2005. The Solar Patrol mission is planned to fly in 2005–2006 aboard the Russian part of the International Space Station (ISS) [*Avahyan and Kuvaldin*, 2000], and it consists of three instruments to measure the solar XUV and EUV irradiance from 0.14 to 153 nm. The SOL-ACES is planning to fly in 2005–2006 as part of the ESA part of the ISS [*Wienhold et al.*, 2000], and it will measure the solar irradiance from 17 to 220 nm using grating spectrometers. The SDO EVE will measure the solar EUV irradiance from 0.1 to 105 nm with 0.1 nm spectral resolution longward of 5 nm and is expected to be launched in 2008.

[109] **Acknowledgments.** We thank the many LASP and JHU/APL staff who fabricated, tested, operated, and continue to operate the SEE instrument and the TIMED spacecraft. We also thank NASA HQ and GSFC for their support of the TIMED program and NSROC and WSMR for their support of the SEE rocket calibration flights. We thank Linton Floyd for providing the updated UARS SUSIM data, Harry Warren for the latest version of the NRLEUV model, and the SOHO EIT team for the solar EUV images used in Figure 8. We also thank the reviewers for their many useful suggestions for this manuscript. This work has been supported by NASA grant NAG5-11408 at the University of Colorado and by NASA grant NAG5-12449 to the University of Alaska. The SEE Level 2 and Level 3 data products can be obtained from the SEE web site at http://lasp.colorado.edu/see/.

[110] Shadia Rifai Habbal thanks Linton Floyd and Douglas J. Strickland for their assistance in evaluating this paper.

## References

Avahyan, S. V., and E. V. Kuvaldin (2000), The results of work creating XUV instrumentation for the Solar Patrol mission, *Phys. Chem. Earth*, *25*, 441.

Bailey, S. M., T. N. Woods, C. A. Barth, S. C. Solomon, L. R. Canfield, and R. Korde (2000), Measurements of the solar soft X-ray irradiance from

the Student Nitric Oxide Explorer: first analysis and underflight calibrations, *J. Geophys. Res.*, *105*, 27,179.

Bailey, S. M., T. N. Woods, C. A. Barth, S. C. Solomon, L. R. Canfield, and R. Korde (2001), Correction to "Measurements of the solar soft X-ray irradiance from the Student Nitric Oxide Explorer: First analysis and underflight calibrations," *J. Geophys. Res.*, *106*, 15,791.

Brace, L. H., W. R. Hoegy, and R. F. Theis (1988), Solar EUV measurements at Venus based on photoelectron emission from the Pioneer Venus Langmuir probe, *J. Geophys. Res.*, *93*, 7282.

Brasseur, G., and S. Solomon (1986), *Aeronomy of the Middle Atmosphere: Chemistry and Physics of the Stratosphere and Mesosphere*, Springer, New York.

Brekke, P., G. J. Rottman, J. Fontenla, and P. G. Judge (1996), The ultraviolet spectrum of a 3B class flare observed with SOLSTICE, *Astrophys. J.*, *468*, 418.

Brueckner, G. E., K. L. Edlow, L. E. Floyd, J. L. Lean, and M. E. VanHoosier (1993), The Solar Ultraviolet Spectral Irradiance Monitor (SUSIM) Experiment on board the Upper Atmospheric Research Satellite (UARS), *J. Geophys. Res.*, *98*, 10,695.

Canfield, L. R., and N. Swanson (1987), Far ultraviolet detector standards, *J. Res. Natl. Bur. Stand.*, *92*, 97.

Canfield, L. R., J. Kerner, and R. Korde (1989), Stability and quantum efficiency performance of silicon photodiode detectors in the far ultraviolet, *Appl. Opt.*, *28*, 3940.

Canfield, L. R., R. Vest, T. N. Woods, and R. Korde (1994), Silicon photodiodes with integrated thin film filters for selective bandpasses in the extreme ultraviolet, *SPIE Proc.*, *2282*, 31.

Chamberlain, J. W. (1978), *Theory of Planetary Atmospheres: An Introduction to Their Physics and Chemistry*, Elsevier, New York.

Chamberlin, P. C., T. N. Woods, and F. G. Eparvier (2004), Rocket Extreme ultraviolet Grating Spectrometer (EGS): Calibrations and results of the solar extreme ultraviolet irradiance on February 8, 2002, *SPIE Proc.*, in press.

Crane, P. C., L. E. Floyd, J. W. Cook, L. C. Herring, E. H. Avrett, and D. K. Prinz (2004), The center-to-limb behavior of solar active regions at ultraviolet wavelengths, *Astron. Astrophys.*, *419*, 735.

Donnelly, R. F. (1976), Empirical models of solar flare X-ray and EUV emissions for use in studying the E and F region effects, *J. Geophys. Res.*, *81*, 4745.

Donnelly, R. F. (1987), Gaps between solar UV & EUV radiometry and atmospheric sciences, in *Solar Radiative Output Variation*, edited by P. Foukal, p. 139, Cambridge Res. and Instrum. Inc, Boulder, Colo.

Donnelly, R. F., and L. C. Puga (1990), Thirteen-day periodicity and the center-to-limb dependence of UV, EUV, and X-ray emission of solar activity, *Solar Phys.*, *130*, 369.

Eparvier, F. G., T. N. Woods, G. Ucker, and D. L. Woodraska (2001), TIMED Solar EUV Experiment: Pre-flight calibration results for the EUV Grating Spectrograph, *SPIE Proc.*, *4498*, 91.

Fontenla, J. M., O. R. White, P. A. Fox, E. H. Avrett, and R. L. Kurucz (1999), Calculation of solar irradiances, I, Synthesis of the solar spectrum, *Astrophys. J.*, *518*, 480.

Garcia, H. (2000), Thermal-spatial analysis of medium and large solar flares, 1976 to 1996, *Astrophys. J. Suppl.*, *127*, 189.

Hall, L. A., and H. E. Hinteregger (1970), Solar radiation in the extreme ultraviolet and its variation with solar rotation, *J. Geophys. Res.*, *75*, 6959.

Hedin, A. E. (1991), Extension of the MSIS thermosphere model into the middle and lower atmosphere, *J. Geophys. Res.*, *96*, 1159.

Heroux, L., and J. E. Higgins (1977), Summary of full-disk solar fluxes between 250 and 1940 A, *J. Geophys. Res.*, *82*, 3307.

Hinteregger, H. E., D. E. Bedo, and J. E. Manson (1973), The EUV Spectrophotometer on Atmosphere Explorer, *Radio Sci.*, *8*, 349.

Hinteregger, H. E., K. Fukui, and G. R. Gilson (1981), Observational, reference and model data on solar EUV from measurements on AE-E, *Geophys. Res. Lett.*, *8*, 1147.

Judge, D. L., et al. (1998), First solar EUV irradiances obtained from SOHO by the CELIAS/SEM, *Solar Phys.*, *177*, 161.

Korde, R., and L. R. Canfield (1989), Silicon photodiodes with stable, near theoretical quantum efficiency in the soft X-ray region, *SPIE Proc.*, *1140*, 126.

Korde, R., and J. Geist (1987), Quantum efficiency stability of silicon photodiodes, *Appl. Opt.*, *26*, 5284.

Korde, R., L. R. Canfield, and B. Wallis (1988), Stable high quantum efficiency silicon photodiodes for vacuum ultraviolet applications, *SPIE Proc.*, *932*, 153.

Lean, J. (1987), Solar ultraviolet irradiance variations: A review, *J. Geophys. Res.*, *92*, 839.

Lean, J. (1991), Variations in the Sun's radiative output, *Rev. Geophys.*, *29*, 505.

Lean, J. L., W. C. Livingston, D. F. Heath, R. F. Donnelly, A. Skumanich, and O. R. White (1982), A three-component model of the variability of the solar ultraviolet flux 145–200 nm, *J. Geophys. Res.*, *87*, 10,307.

Lean, J. L., G. J. Rottman, H. L. Kyle, T. N. Woods, J. R. Hickey, and L. C. Puga (1997), Detection and parameterization of variations in solar mid and near ultraviolet radiation (200 to 400 nm), *J. Geophys. Res.*, *102*, 29,939.

Lean, J. L., H. P. Warren, J. T. Mariska, and J. Bishop (2003), A new model of solar EUV irradiance variability: 2. Comparisons with empirical models and observations and implications for space weather, *J. Geophys. Res.*, *108*(A2), 1059, doi:10.1029/2001JA009238.

McClintock, W. E., C. A. Barth, R. E. Steele, G. M. Lawrence, and J. G. Timothy (1982), Rocket-borne instrument with a high-resolution microchannel plate detector for planetary UV spectroscopy, *Appl. Opt.*, *21*, 3071.

Meier, R. R., et al. (2002), Ionospheric and dayglow effects caused by the radiative phase of the Bastille Day flare, *Geophys. Res. Lett.*, *29*(10), 1461, doi:10.1029/2001GL013956.

Mewe, R., and E. H. B. M. Gronenschild (1981), Calculated X-radiation from optically thin plasmas. IV - Atomic data and rate coefficients for spectra in the range 1–270 Å, *Astron. Astrophys. Suppl, Ser.*, *45*, 11.

Mewe, R., E. H. B. M. Gronenschild, and G. H. J. van den Oord (1985), Calculated X-radiation from optically thin plasmas. V, *Astron. Astrophys. Suppl, Ser.*, *62*, 197.

Mewe, R., J. R. Lemen, and G. H. J. van den Oord (1986), Calculated X-radiation from optically thin plasmas. VI - Improved calculations for continuum emission and approximation formulae for nonrelativistic average Gaunt factors, *Astron. Astrophys.*, *65*, 511.

Ogawa, H. S., L. R. Canfield, D. McMullin, and D. L. Judge (1990), Sounding rocket measurement of the absolute solar EUV flux utilizing a silicon photodiode, *J. Geophys. Res*, *95*, 4291.

Oster, L. (1983), Solar irradiance variations: 2. Analysis of the Extreme Ultraviolet Spectrometer measurements onboard the Atmospheric Explorer E satellite, *J. Geophys. Res*, *88*, 9037.

Pap, J. M., C. Fröhlich, H. S. Hudson, and S. K. Solanki (Eds.) (1994), *The Sun as a Variable Star: Solar and Stellar Irradiance Variations*, Cambridge Univ. Press, New York.

Parr, A. C., and S. Ebner (1987), *SURF II User Handbook*, *NBS Spec. Publ.*, Natl. Bur. of Stand., Gaithersburg, Md.

Picone, M. J., A. E. Hedin, D. P. Drob, and A. C. Aikin (2002), NRLMSISE-00 empirical model of the atmosphere: Statistical comparisons and scientific issues, *J. Geophys. Res.*, *107*(A12), 1468, doi:10.1029/2002JA009430.

Powell, F. R., P. W. Vedder, J. F. Lindblom, and S. F. Powell (1990), Thin film filter performance for extreme ultraviolet and X-ray applications, *Opt. Eng.*, *26*, 614.

Reeves, E. M., and W. H. Parkinson (1970), An atlas of extreme-ultraviolet spectroheliograms from OSO-IV, *Astrophys. J. Suppl.*, *181*, 1.

Richards, P. G., J. A. Fennelly, and D. G. Torr (1994), EUVAC: A solar EUV flux model for aeronomic calculations, *J. Geophys. Res.*, *99*, 8981.

Roble, R. G. (1976), Solar EUV variation during a solar cycle as derived from ionospheric modeling considerations, *J. Geophys. Res.*, *81*, 265.

Roble, R. G., E. C. Ridley, A. D. Richmond, and R. E. Dickinson (1988), A coupled thermosphere/ionosphere general circulation model, *Geophys. Res. Lett.*, *15*, 1525.

Rottman, G. J. (1987), Results from space measurements of solar UV and EUV flux, in *Solar Radiative Output Variation*, edited by P. Foukal, p. 71, Cambridge Res. and Instrum. Inc, Boulder, Colo.

Rottman, G. J., T. N. Woods, and T. P. Sparn (1993), Solar Stellar Irradiance Comparison Experiment 1: 1. Instrument design and operation, *J. Geophys. Res.*, *98*, 10,667.

Schmidtke, G., P. Seidl, and C. Wita (1985), Airglow-solar spectrometer instrument (20–700 nm) aboard the San Marco D/L satellite, *Appl. Opt.*, *24*, 3206.

Schmidtke, G., T. N. Woods, J. Worden, G. J. Rottman, H. Doll, C. Wita, and S. C. Solomon (1992), Solar EUV irradiance from the San Marco ASSI: A reference spectrum, *Geophys. Res. Lett.*, *19*, 2175.

Scholze, F., R. Thornagel, and G. Ulm (2001), Calibration of energy-dispersive X-ray detectors at BESSY I and BESSY II, *Metrologia*, *38*, 391.

Simon, P. (1983), The solar cycle, *L'Astronomie*, *97*, 526.

Solomon, S. C., S. M. Bailey, and T. N. Woods (2001), Effect of solar soft X-rays on the lower ionosphere, *Geophys. Res. Lett.*, *28*, 2149.

Strickland, D. J., J. L. Lean, R. R. Meier, A. B. Christensen, L. J. Paxton, D. Morrison, J. D. Craven, R. L. Walterscheid, D. L. Judge, and D. R. McMullin (2004), Solar EUV irradiance variability derived from terrestrial far ultraviolet dayglow observations, *Geophys. Res. Lett.*, *31*, L03801, doi:10.1029/2003GL018415.

Tobiska, W. K. (1991), Revised solar extreme ultraviolet flux model, *J. Atmos. Terr. Phys.*, *53*, 1005.

Tobiska, W. K. (1993), Recent solar extreme ultraviolet irradiance observations and modeling: A review, *J. Geophys. Res.*, *98*, 18,879.
Tobiska, W. K., and C. A. Barth (1990), A solar EUV flux model, *J. Geophys. Res.*, *95*, 8243.
Tobiska, W. K., and F. G. Eparvier (1998), EUV97: Improvements to EUV irradiance modeling in the soft X-rays and FUV, *Solar Phys.*, *177*, 147.
Tobiska, W. K., T. N. Woods, F. G. Eparvier, R. Viereck, L. Floyd, D. Bouwer, G. J. Rottman, and O. R. White (2000), The SOLAR2000 empirical solar irradiance model and forecast tool, *J. Atmos. Sol. Terr. Phys.*, *62*, 1233.
Torr, M. R., and D. G. Torr (1985), Ionization frequencies for solar cycle 21: Revised, *J. Geophys. Res.*, *90*, 6675.
Walker, J. H., R. D. Saunders, J. K. Jackson, and D. A. McSparron (1988), The NBS scale of spectral irradiance, *J. Res. Natl. Bur. Stand.*, *93*, 7.
Warren, H. P., J. T. Mariska, and J. Lean (1998a), A new reference spectrum for the EUV irradiance of the quiet Sun: 1. Emission measure formulation, *J. Geophys. Res.*, *103*, 12,077.
Warren, H. P., J. T. Mariska, and J. Lean (1998b), A new reference spectrum for the EUV irradiance of the quiet Sun: 2. Comparisons with observations and previous models, *J. Geophys. Res.*, *103*, 12,091.
Warren, H. P., J. T. Mariska, and J. Lean (2001), A new model of solar EUV irradiance variability: 1. Model formulation, *J. Geophys. Res.*, *106*, 15,745.
White, O. R. (Ed.) (1977), *The Solar Output and Its Variation*, Colorado Assoc. Univ. Press, Boulder.
Wienhold, F. G., J. Anders, B. Galuska, U. Klocke, M. Knothe, W. J. Riedel, G. Schmidtke, R. Singler, U. Ulmer, and H. Wolf (2000), The Solar package on ISS: SOL-ACES, *Phys. Chem. Earth*, *25*, 473.
Woods, T. (1992), Working group 4 and 5 report for 1991 SOLERS 22 workshop, in *Proceedings of SOLERS 22 Workshop*, edited by D. Donnelly, p. 460, Natl. Ocean. and Atmos. Admin., Boulder, Colo.
Woods, T. N., and G. J. Rottman (1990), Solar EUV irradiance derived from a sounding rocket experiment on 10 November 1988, *J. Geophys. Res.*, *95*, 6227.
Woods, T. N., and G. J. Rottman (2002), Solar ultraviolet variability over time periods of aeronomic interest, in *Atmospheres in the Solar System: Comparative Aeronomy*, *Geophys. Monogr. Ser.*, vol. 130, edited by M. Mendillo, A. Nagy, and J. H. Waite Jr., p. 221, AGU, Washington, D. C.
Woods, T. N., G. J. Ucker, and G. J. Rottman (1993), Solar Stellar Irradiance Comparison Experiment I: 2. Instrument calibration, *J. Geophys. Res.*, *98*, 10,679.
Woods, T. N., R. T. Wrigley, G. J. Rottman, and R. E. Haring (1994), Scattered light properties of diffraction gratings, *Appl. Opt.*, *33*, 4273.
Woods, T. N., et al. (1996), Validation of the UARS solar ultraviolet irradiances: Comparison with the ATLAS 1 and 2 measurements, *J. Geophys. Res.*, *101*, 9541.
Woods, T., F. Eparvier, S. Bailey, S. C. Solomon, G. Rottman, G. Lawrence, R. Roble, O. R. White, J. Lean, and W. K. Tobiska (1998), TIMED Solar EUV Experiment, *SPIE Proc.*, *3442*, 180.
Woods, T., E. Rodgers, S. Bailey, F. Eparvier, and G. Ucker (1999a), TIMED Solar EUV Experiment: Pre-flight calibration results for the XUV Photometer System, *SPIE Proc.*, *3756*, 255.
Woods, T., G. Rottman, C. Russell, and B. Knapp (1999b), In-flight degradation results for the UARS SOLSTICE instrument, *Metrologia*, *35*, 619.
Woods, T. N., W. K. Tobiska, G. J. Rottman, and J. R. Worden (2000a), Improved solar Lyman $\alpha$ irradiance modeling from 1947 through 1999 based on UARS observations, *J. Geophys. Res.*, *105*, 27,195.
Woods, T., G. Rottman, J. Harder, G. Lawrence, B. McClintock, G. Kopp, and C. Pankratz (2000b), Overview of the EOS SORCE mission, *SPIE Proc.*, *4135*, 192.
Woods, T. N., S. M. Bailey, W. K. Peterson, H. P. Warren, S. C. Solomon, F. G. Eparvier, H. Garcia, C. W. Carlson, and J. P. McFadden (2003), Solar extreme ultraviolet variability of the X-class flare on 21 April 2002 and the terrestrial photoelectron response, *Space Weather*, *1*(1), 1001, doi:10.1029/2003SW000010.
Woods, T. N., et al. (2004a), Solar extreme ultraviolet and X-ray irradiance variations, in *Solar Variability and Its Effect on Climate*, *Geophys. Monogr. Ser.*, vol. 141, edited by J. Pap et al., p. 147, AGU, Washington, D. C.
Woods, T. N., F. G. Eparvier, J. Fontenla, J. Harder, G. Kopp, W. E. McClintock, G. Rottman, B. Smiley, and M. Snow (2004b), Solar irradiance variability during the October 2003 solar storm period, *Geophys. Res. Lett.*, *31*, L10802, doi:10.1029/2004GL019571.
Worden, J. R., O. R. White, and T. N. Woods (1998), Evolution of chromospheric structures derived from Ca II K spectroheliograms: Implications for solar ultraviolet irradiance variability, *Astrophys. J.*, *496*, 998.
Worden, J., T. N. Woods, W. M. Neupert, and J. P. Delaboundiniere (1999), Evolution of chromospheric structures: How chromospheric structures contribute to the solar He II 30.4 nanometer irradiance and variability, *Astrophys. J.*, *511*, 965.

S. M. Bailey, University of Alaska, 903 Koyukuk Dr., Fairbanks, AK 99775-7320, USA.
P. C. Chamberlin, F. G. Eparvier, G. J. Rottman, D. L. Woodraska, and T. N. Woods, Laboratory for Atmospheric and Space Physics, University of Colorado, 1234 Innovation Dr., Boulder, CO 80303, USA. (tom.woods@lasp.colorado.edu)
J. Lean, Naval Research Laboratory, 4555 Overlook Ave., SW, Washington, DC 20375-5000, USA.
S. C. Solomon, National Center for Atmospheric Research, 3450 Mitchell Lane, Boulder, CO 80301, USA.
W. K. Tobiska, Space Environment Technologies, 1676 Palisades Dr., Pacific Palisades, CA 90272-2111, USA.